Cell Communication and Signaling

https://doi.org/10.1186/s12964-026-02862-8

Article in Press

Clinical and molecular characterization of a novel pathogenic AIFM1 E336K mutation connecting mitochondrial dysfunction and neurodegeneration

Received: 9 December 2025

Accepted: 28 March 2026

Published online: 09 April 2026

Cite this article as: Ferrer M., Pedrón M., Soriano O. *et al.* Clinical and molecular characterization of a novel pathogenic AIFM1 E336K mutation connecting mitochondrial dysfunction and neurodegeneration. *Cell Commun Signal* (2026). https://doi.org/10.1186/s12964-026-02862-8

Miguel Ferrer, María Pedrón, Olga Soriano, Marta Martínez-Julvez, Mikel Marín-Baquero, Rut García-Villanueva, Adrián Velázquez-Campoy, Joaquín Marco-Brualla, Cristina Ripollés-Yuba, Patricio Fernández-Silva, Milagros Medina, María Dolores Miramar, María Bestué, Raquel Moreno-Loshuertos & Patricia Ferreira

To submit to Cell Communication and Signaling

Clinical and molecular characterization of a novel pathogenic AIFM1 E336K mutation connecting mitochondrial dysfunction and neurodegeneration

Miguel Ferrer[1,2#†], María Pedrón[1†], Olga Soriano[1,2], Marta Martínez-Julvez[1,2], Mikel Marín-Baquero[1], Rut García-Villanueva[1,2], Adrián Velázquez-Campoy[1,2,3,4], Joaquín Marco-Brualla[1,5], Cristina Ripollés-Yuba[1], Patricio Fernández-Silva[1,2], Milagros Medina[1,2], María Dolores Miramar[6], María Bestué[7], Raquel Moreno-Loshuertos[1,2*] and Patricia Ferreira[1,2*]

[1]Departamento de Bioquímica y Biología Molecular y Celular, Facultad de Ciencias, Universidad de Zaragoza, Zaragoza, Spain

[2]Instituto de Biocomputación y Física de Sistemas Complejos, BIFI (GBsC-CSIC Joint Unit), Universidad de Zaragoza, Zaragoza, Spain

[3]Institute for Health Research Aragon (IIS Aragon), Zaragoza, Spain

[4]Biomedical Research Networking Center in Hepatic and Digestive Diseases (CIBERehd), Madrid, Spain

[5]Faculty of Pharmacy, University San Pablo-CEU, 28660 Boadilla del Monte, Spain

[6]Servicio de Genética, Hospital Universitario Miguel Servet, Zaragoza, España

[7]Servicio de Neurología, Hospital Universitario Miguel Servet, Zaragoza, España

To submit to Cell Communication and Signaling

[†]These authors contributed equally to this work

[#]Current address: Departamento de Ciencia Vegetal, Centro de Investigación y Tecnología Agroalimentaria de Aragón (CITA). Instituto Agroalimentario de Aragón-IA2, CITA-Universidad de Zaragoza, Zaragoza, Spain

[*]**Correspondence:**

Raquel Moreno-Loshuertos

raquelml@unizar.es

Patricia Ferreira

ferreira@unizar.es

Abstract

Mutations in the *AIFM1* gene, encoding the apoptosis-inducing factor (AIF), have been associated with a spectrum of neurometabolic disorders. However, the mechanistic basis underlying their pathogenicity remains poorly understood. In this work, we identified and comprehensively characterized a novel hemizygous *AIFM1* mutation c.1006G>A (E336K) in a male patient presenting with a progressive hereditary axonal sensorimotor polyneuropathy with childhood onset, inherited in an X-linked recessive pattern, associated with sensorineural hearing loss and without cognitive impairment. The clinical phenotype was consistent with Charcot-Marie-Tooth disease type 4 (CMTX4). Patient-derived fibroblasts exhibited reduced AIF protein stability despite preserved mRNA expression, impaired growth

in OXPHOS-dependent conditions, decreased basal respiration, and altered assembly of mitochondrial respiratory supercomplexes. These defects were accompanied by reduced CHCHD4 protein levels and mitochondrial content. The purified E336K protein exhibited compromised FAD retention, decreased thermal stability, impaired NADH affinity, destabilization of the charge-transfer complex crucial for sustaining the AIF:CHCHD4 interaction, and a shift in coenzyme preference toward NADPH. Structurally, the substitution of Glu336 with Lys remodels the electrostatic environment of the NADH-binding cleft, thereby compromising redox function and weakening CHCHD4 binding. Despite these defects, the protein with the E336K mutation retained DNA binding, nuclease activity, and binding to nuclear partners, although parthanatos induction was attenuated in patient fibroblasts. Collectively, these molecular alterations converge on defective mitochondrial bioenergetics and dynamics, providing a direct mechanistic link to the patient's clinical evolution.

These findings provide a framework for understanding *AIFM1*-related disorders and pave the way for the development of future personalized molecular therapies.

Introduction

The human apoptosis-inducing factor (hAIF), encoded by the *AIFM1* (Apoptosis Inducing Factor Mitochondria Associated 1) gene on chromosome Xq25, is a mitochondrial flavoprotein with dual roles in

energy metabolism and caspase-independent programmed cell death [47]. Under physiological conditions, AIF is anchored to the inner mitochondrial membrane, where it functions as a FAD-dependent NADH oxidoreductase essential for mitochondrial morphology, redox homeostasis, and the biogenesis and stability of the oxidative phosphorylation system (OXPHOS) complexes, particularly complexes I and III and complex IV subunits and assembly factors [12, 22, 31, 50, 56].

Structurally, AIF comprises an N-terminal mitochondrial targeting sequence, a central oxidoreductase domain with FAD- and NADH-binding motifs, and a C-terminal domain required for NADH-dependent dimerization and apoptotic activity [20]. These modular domains allow AIF to act as an NADH/NAD^+ redox sensor, switching from a metabolic supporter to a death effector in response to cellular stress. NADH binding and its oxidation by the AIF flavin cofactor induce the formation of a stable reduced isoalloxazine:NAD^+ charge-transfer complex (CTC) with FAD, triggering conformational rearrangements that displace the regulatory C-terminal loop (residues 509-559), promoting dimerization, and facilitating interaction with Coiled-Coil-Helix-Coiled-Coil-Helix Domain-Containing Protein 4 (CHCHD4), a central component of the mitochondrial disulfide relay system [6, 20, 22, 38]. Through this long-lived interaction, reduced and dimeric AIF supports the import and folding of CHCHD4-dependent substrates, including complex I and complex IV subunits and thereby supporting respiratory chain assembly [9, 26, 42]. Disruption of this pathway leads to mitochondrial

dysfunction, redox imbalance, and, in animal models, embryonic lethality [13, 29, 42].

Beyond its metabolic function, AIF mediates large-scale DNA fragmentation and chromatin condensation in response to severe genotoxic stress, in a caspase-independent process known as parthanatos [5, 47]. This apoptogenic function requires the proteolytic cleavage and nuclear translocation of AIF, events favored by redox-sensitive conformational changes in the protein upon NADH depletion [35, 47]. AIF, thus, lies at the intersection of mitochondrial bioenergetics and programmed cell death pathways.

Pathogenic variants in *AIFM1* were first reported in 2010, with the identification of a hemizygous deletion (ΔR201) in a male patient with severe mitochondrial encephalopathy [21]. Since then, an expanding phenotypic spectrum has been linked to *AIFM1* mutations, including X-linked Charcot-Marie-Tooth disease type 4 (CMTX4/COWCK) [40, 53] (also referred to as Cowchock syndrome, after the author who first described a family with this phenotype in 1985) [10], combined oxidative phosphorylation deficiency 6 (COXPD6) [4], auditory neuropathy spectrum disorder (DFNX5) [58] and Severe Encephalomyopathy with Developmental Delay, Hypotonia, and Lactic Acidosis (SEMDHL) [32] (Table 1 and S1). Most pathogenic variants cluster within the FAD- and NADH-binding domains, pointing to a central role of redox balance impairment in disease pathogenesis. Nonetheless, most variants remain poorly characterized at the

functional and molecular levels and the mechanistic basis underlying their pathogenicity remains unknown.

Here, we report the identification and functional characterization of a novel *AIFM1* missense variant, E336K, in a male patient exhibiting a neurodegenerative phenotype consistent with Cowchock syndrome. This E336K mutation is located in the AIF NADH-binding domain, where residue E336 lies within a highly conserved structural region essential for NADH coordination and redox cycling [20, 46]. We have comprehensively characterized this mutation from an integrated, multi-level perspective –spanning longitudinal clinical and neurological follow-up, molecular and cellular functional studies, and structural–biophysical analyses. By directly linking the patient's clinical evolution to the underlying molecular defect, we elucidate the pathogenic mechanism of the E336K variant and establish a model for genotype–phenotype correlations in *AIFM1*-related disorders. This integrative approach deepens our understanding of AIF biology and will surely contribute to facilitating rational developments in future precision molecular therapies.

Material and Methods

Patients and clinical evaluations

Clinical data were collected from a family originating from northern Spain (Aragón) spanning three generations with a phenotype consistent with CMTX4. Two brothers were clinically affected; their

mother and the daughter of one affected patient were also carriers. Genetic testing results were available for all family members except for one clinically affected brother. This relative presented clinically with a polyneuropathy; however, his evaluations were not included, as he declined follow-up and further investigations.

For one of the affected patients, complete clinical information was obtained, and longitudinal follow-up was carried out by the Neuromuscular Unit at Hospital Universitario Miguel Servet from June 2016 to June 2024. In May 2023, the patient was enrolled in the research project *Flavoenzymes in Health, Diseases and Drug Discovery* conducted by the University of Zaragoza (Hospital Miguel Servet, Department of Biochemistry, Molecular and Cell Biology, Faculty of Sciences, and the Institute for Biocomputation and Complex Systems Physics). As part of this study, blood and skin tissue samples were obtained, the latter through a skin biopsy. No muscle tissue was collected, as the patient declined to undergo a muscle biopsy.

From the electronic medical record, the following evaluations were retrieved: laboratory tests: complete blood count (CBC), chemistry, coagulation, lactic acid, autoantibodies, vitamin E, creatine kinase (CK), long-chain fatty acids and thyroid hormone. Brain and acoustic nerve MRI, brainstem auditory evoked potentials (BAEPs), serial audiometries, echocardiogram and Holter monitoring, as well as multidisciplinary assessments by cardiology and otorhinolaryngology services, in addition to annual follow-up by neurology. A neurophysiological study was performed to confirm the neuropathy

phenotype using a Synergy 28 system. Motor and sensory nerve conduction studies were performed in the median and ulnar nerves of the upper limbs. In the lower limbs, motor conduction studies were carried out in the peroneal and tibial nerves, and sensory studies in the superficial peroneal and sural nerves. The assessment was completed with an electromyographic evaluation, as shown in Table 2**.**

Written informed consent was obtained from the patient for participation in the study, for the performance of the skin biopsy, and for publication of the results.

Genetic/Mutational analysis

A comprehensive exome sequencing analysis was performed on the DNA sample extracted from peripheral blood, with the aim of identifying genomic variants in 53 genes associated with Charcot-Marie-Tooth disease and related hereditary sensorimotor neuropathies (NIMGenetics). The panel used for library preparation was designed using Ion AmpliSeq™ Exome technology (Life Technologies), capturing >97% of CCDS (>19,000 genes, >198,000 exons, >85% of alterations responsible for genetic diseases) and flanking splice regions (5 bp). It has a size of ~33 Mb and comprises a total of 293,903 amplicons. Library sequencing was performed on a next-generation high-throughput sequencer, the Ion Proton™ (Life Technologies). In the study conducted, a mean coverage depth of 79X was obtained. A total of 1177 amplicons covering the selected genes in this panel were analyzed. 96% of the amplicons included in the study had a read depth

greater than 20X. The obtained sequences were aligned to the reference genome (build 37 of the human genome, Hg19) using the TMAP Ion Alignment software. The aligned and filtered sequences, according to specific quality criteria, were analyzed to identify nucleotide variations with respect to the reference genome (VariantCaller). Variant annotation was performed with Ion Reporter (Life Technologies). The analysis focused on identifying variants located in exonic regions or splice regions, which imply a change at the protein level (missense or nonsense mutations, and nucleotide insertions, deletions, or indels), and which present at a frequency higher than 40% of the reads. The list of identified variants was evaluated using information from databases (http://www.ncbi.nlm.nih.gov/SNP/, http://www.1000genomes.org, http://evs.gs.washington.edu/EVS, http:// https://www.ncbi.nlm.nih.gov/clinvar/, https://varsome.com/, https://franklin.genoox.com/clinical-db/home, https://databases.lovd.nl/shared/genes). Furthermore, the functional effect of genomic variations classified as pathogenic was assessed using 9 prediction systems (SIFT, PROVEAN, PolyPhen2, MutationTaster, MutationAssessor, LRT, FATHMM, MetaSVM, and CONDEL) included in the ALAMUT analysis package (http://www.interactive-bioware.com) and the ANNOVAR package (http://www.openbioinformatics.org/annovar/). Finally, the association of the identified mutations with OMIM syndromes was evaluated. Sanger sequencing of the genomic fragment chrX:129271006-

129271226 was performed on the familial DNA samples (brother, Labgenetics; mother and daughter, NIMGenetics) to identify the *AIFM1* variant c.1006G>A; p.Glu336Lys.

Cell culture

Control and mutant human fibroblasts were obtained from skin biopsies from a 38-year-old healthy donor and a 55-year-old patient with X-linked Charcot-Marie-Tooth disease carrying a single mutation, c.1006G>A (p. Glu336Lys), in the AIF gene, respectively. Skin biopsies were collected with informed consent in accordance with institutional ethical guidelines and under approved protocols. Biopsy samples were sterilized with ethanol, rinsed with sterile PBS and mechanically disaggregated into ~1 mm^2 pieces using forceps and a scalpel. The tissue fragment was then transferred to 15 mL Corning tubes containing 5 mL of high-glucose DMEM supplemented with 20 % fetal bovine serum (FBS, GIBCO), 1 % penicillin-streptomycin (GIBCO), and 1 mL of collagenase I (4 mg/mL). Samples were incubated overnight at 37 °C in a 5 % CO_2 atmosphere. Following enzymatic digestion, cells and residual tissue were centrifuged at 1,500 g for 10 minutes. The resulting pellet was washed with sterile PBS and centrifuged three times under the same conditions. Finally, the pellet was resuspended in high-glucose DMEM supplemented with 20 % FBS and seeded in 60 mm culture dishes. Primary cultures were immortalized at passage 4 by transduction with the lentiviral plasmid pLOX-Ttag-iresTK (Tronolab). Once exponential growth was established, the FBS

concentration in the culture medium was reduced to 10 %. To minimize clonal artifacts and potential biases derived from selection of individual clones, phenotypic characterization of mutant and control cell lines was performed using polyclonal cell populations.

Growth measurements

Growth rate in galactose-containing medium was determined by seeding 5 x 10^4 cells per well on 12-well plates with 2 mL of either high-glucose DMEM supplemented with 10% FBS, or glucose-free DMEM supplemented with 0.9 mg /mL galactose,1 mM sodium pyruvate, and 10 % FBS. Cells were incubated at 37 °C for 5 days, and cell numbers were recorded every 24 hours.

Cell Viability Assays

The relative growth of different cell lines in response to oxidative phosphorylation (OXPHOS) inhibitors was evaluated using the MTT (3-(4,5-dimethylthiazol-2-yl)-2,5-diphenyltetrazolium bromide) reduction assay, following the method described by Mosmann T. [33]. Briefly, 1×10^4 cells per well were plated in 96-well flat-bottom plates and cultured in galactose-containing medium in the presence of two concentrations of rotenone (2 and 10 nM), antimycin A (2 and 10 nM), or sodium azide (20 and 100 µM) for 48 h at 37 °C. After drug exposure, cells were incubated with fresh medium containing 1 mg/mL MTT for 4 h at 37 °C in a humidified atmosphere. Formazan crystals were dissolved in DMSO, and the absorbance was measured at 570 nm using

a microplate reader. Results were expressed as percentages relative to untreated control cells. All experiments were performed at least in triplicate.

Oxygen consumption measurements

Endogenous and maximal O_2 consumption in intact cells was measured using an Oxytherm Clark-type electrode (Hansatech), as previously described [24], with minor modifications [1].

Enzymatic activities analysis

Spectrophotometric measurements of the enzymatic activity of OXPHOS complexes were performed in cell homogenates obtained from digitonin-permeabilized fibroblasts using a thermostated microplate reader, as previously described [48]. All activities were evaluated at 30 ºC except for complex IV (CIV), which was measured at 38 ºC. Rotenone-sensitive NADH dehydrogenase activity (Complex I, CI) was measured at 340 nm (ε= 6.22 $mM^{-1} \cdot cm^{-1}$) in a reaction mixture containing 20 mM potassium phosphate buffer (pH 8.0), 0.2 mM NADH, 1 mM NaN_3, 1 mg/mL fatty acid-free BSA (prepared in 10 mM EDTA, pH 7.4) and 50 µM ubiquinone-1 (UQ_1). Rotenone sensitivity was determined under the same conditions in the presence of 5 µM rotenone. Cytochrome c oxidase activity (COX, CIV) was measured at 550 nm (ε= 21 $mM^{-1} \cdot cm^{-1}$) in a reaction mixture containing 50 mM potassium phosphate (pH 7.0) and freshly reduced cytochrome c (100 µM). NADH-cytochrome c oxidoreductase (CI+III) and succinate-

cytochrome c oxidoreductase (CII+III) activities were assessed at 550 nm (ε= 21 $mM^{-1} \cdot cm^{-1}$) in a reaction mixture containing 20 mM potassium phosphate buffer (pH 8.0), 0.2 mM cytochrome c, 1 mM NaN_3, 1 mg/mL fatty acid-free BSA (prepared in 10 mM EDTA, pH 7.4), supplemented with either 100 µM NADH (for CI+III) or 3 mM sodium succinate (for CII+III). Citrate synthase activity was measured at 412 nm (ε= 13.6 $mM^{-1} \cdot cm^{-1}$) in a reaction mixture containing 75 mM Tris-HCl 10 mM (pH 8.0), 0.4 mM acetyl-CoA, 0.1 mM DTNB (5,5-dithio-bis-2-nitrobenzoic acid), 0.5 mM oxaloacetate and 0.1 % Triton X-100.

Evaluation of protein expression

For preparation of total cell protein extracts, cells were harvested from 60 mm-diameter culture plates, washed twice with PBS, and lysed in RIPA buffer (50 mM Tris-HCl pH 7.4, 5 mM EDTA, 1 % Triton X-100, 0.5 % sodium deoxycholate, 50 mM NaCl) containing 1x cOmplete™ Protease Inhibitor Cocktail (Roche). Steady-state levels of proteins, including AIF, CHCHD4 or subunits of the mitochondrial respiratory chain complexes were estimated by loading 60 µg of total protein per lane onto SDS-PAGE gels. Proteins were separated on 12% acrylamide/bisacrylamide gels and electroblotted onto PVDF membranes. Western blotting was performed using specific primary antibodies against human AIF (SIGMA, Cat # A7549, dilution 1:20,000), CHCHD4 (Proteintech, Cat # 21090-1-AP, dilution 1:4,000), β-actin (SIGMA, Cat # A2066 dilution 1:2,000), as well as antibodies targeting complex I (anti-NDUFA9, NADH dehydrogenase (ubiquinone) 1 alpha

subcomplex subunit 9, Invitrogen, Cat # 459100, dilution 1:5,000; NDUFS3, NADH:ubiquinone oxidoreductase core subunit S3, Invitrogen Invitrogen, Cat # 459130, dilution 1:5,000), complex II (anti-70 kDa subunit, SDHA, succinate dehydrogenase complex subunit A, Invitrogen, Cat # 459200, dilution 1:5,000), complex III (anti-UQCRC1, ubiquinol-cytochrome c reductase core protein 1 Invitrogen, Cat # 459140, dilution 1:5,000) and complex IV (anti-MTCO1, cytochrome c oxidase I) Invitrogen, Cat # 459600, dilution 1:10,000). Detection was carried out using HRP-conjugated secondary antibodies (anti-mouse (Cat # 31430, dilution 1:5,000) or anti-rabbit, (Cat # 31460, dilution 1:5,000), Invitrogen) and the Pierce™ ECL Western Blotting Substrate (Thermo Scientific).

Native polyacrylamide electrophoresis analysis of respiratory supercomplexes

Mitochondria were isolated from cultured cell lines according to Schägger [45], with minor modifications [2]. Digitonin-solubilized mitochondrial proteins (60-100 µg per sample) were separated by BN-PAGE using commercial native 3-12 % acrylamide gradient gels (Novex). The assembly of respiratory supercomplexes was analysed by Western Blot (WB) after transfer and detection with specific antibodies.

Mitochondrial Superoxide production and mitochondrial content analysis

To assess mitochondrial ROS production and mitochondrial content, cells were stained with either MitoSOX™ Red (5 µM, Invitrogen) or MitoTracker™ Green FM (200 nM, Invitrogen) for 30 min at 37 ºC. Mean fluorescence intensity was measured by flow cytometry using a FACSCalibur cytometer (BD Biosciences), and data were analyzed using FlowJo Software, version 10.8.1.

Quantitative PCR determination of mRNA transcripts

Total RNA was isolated from 5 x 10^6 cells using TRIzol™ reagent (Invitrogen), and 1 µg of RNA was reverse transcribed into cDNA using the Transcriptor First Strand cDNA Synthesis Kit (Roche). Transcript levels of human *AIF,* mitochondrial superoxide dismutase 2 (*SOD2*) and *CHCHD4* were quantified by qPCR using a LightCycler System (Roche) with the LightCycler Fast-Start DNA MasterPLUS SYBR Green I Kit (Roche), following the manufacturer's recommendations. Transcript levels were normalized to *ACTB* mRNA (NM_007393). Primer sequences are provided in Table S2.

AIF induced cell death analysis

AIF-mediated cell death was analyzed by simultaneous annexin-V and 7AAD staining and flow cytometry, after cell death induction with methylnitronitrosoguanidine (MNNG) as previously described [5]. Briefly, control and mutant cells were grown to a 70 % confluence, and exposed to MNNG (0.5 µM) for 20 min. After treatment, the medium was replaced, and cells were incubated for 24 h at 37 °C in a humidified

atmosphere with 5 % CO_2. Cells were then collected, stained with annexin-V-FITC and 7-AAD (Sigma) for 10 min in annexin binding buffer (140 mM NaCl, 2.5 mM $CaCl_2$, 10 mM HEPES/NaOH, pH 7.4), and analyzed using a FACSCalibur flow cytometer (BD Biosciences, Madrid, Spain). Similar to previous sections, collected data were further processed by using FlowJo software, version 10.8.1.

Recombinant protein expression and purification

Constructs for WT, $AIF_{\Delta 77}$ and $AIF_{\Delta 101}$ and overexpression protocols were previously reported [36, 41, 52]. The genes encoding the human AIF mutation $E336K_{\Delta 77}$ and $E336K_{\Delta 101}$ were obtained by site-directed mutagenesis from GenScript® and subsequently subcloned between the NcoI and NdeI sites of the pET-28a(+) expression vector. WT AIF as well as both the apoptotic $E336K_{\Delta 101}$ and soluble mitochondrial $E336K_{\Delta 77}$ variants, along with CHCHD4 (UniProtKB Q8N4Q1) were heterologously expressed as recombinant proteins carrying an N-terminal removable His_6-tag (CACCAT) using the pET28a(+) expression vector. Expression was performed in *Escherichia coli* C41 (DE3) strain, except for CHCHD4, which was expressed in Shuffle T7 cells to enhance disulfide bond formation.

The production of $E336K_{\Delta 77}$ was performed by growing transformed cells in 2xYT medium containing 30 mg/L kanamycin (Sigma-Aldrich), supplemented with 8 mg/L of riboflavin (Sigma-Aldrich) at 37 °C and 180 r.p.m. until OD_{600nm}~0.5. Then, cultures were induced with 0.5 mM IPTG (Glentham Life Sciences) and incubated 24h under the same

conditions. For $AIF_{\Delta 101}$, cells were grown as previously described [41]. After the cells were harvested, both $E336K_{\Delta 77}$ and $E336K_{\Delta 101}$ variants were purified as previously reported for the apoptotic $WT_{\Delta 101}$ form [41]. CHCHD4 production and purification were performed as formerly described [17]. WT AIF concentrations were determined using the molar absorptivity coefficient previously reported [20]. For $E336K_{\Delta 101}$ this value was estimated by protein denaturation by boiling for 5 minutes at 100 ºC, followed by quantification of the released FAD after a 3-minute centrifugation. The extinction coefficients, $\varepsilon_{452\ nm}$, for $WT_{\Delta 101}$ and $E336K_{\Delta 101}$ variants were 13.7, and 14.6 $M^{-1}{\cdot}cm^{-}1$, respectively. CHCHD4 concentrations were calculated through its theoretical $\varepsilon_{280\ nm}$ value (13.3 $mM^{-1}{\cdot}cm^{-1}$) obtained from the ProtParam tool (ExPASy). All proteins were stored in 50 mM potassium phosphate, pH 7.4 at -80 ºC.

Molecular weight determination by size exclusion chromatography

The $AIF_{\square 101}$ variants, in the absence or presence of 2 mM of NADH and/or CHCHD4, were loaded onto a Superdex 200 increase 10/300 GL (Cytiva) column attached to an ÄKTA go system (Cytiva). $AIF_{\square 101}$:CHCHD4 mixtures (1:3 molar ratio with respect to AIF) were preincubated in 50 mM phosphate buffer pH 7.4, without or with NADH, for 10 min at RT before loading onto the column. Protein elution was carried out in 50 mM phosphate buffer, 150 mM NaCl, pH 7.4, at a flow rate of 0.4 mL/min. Column calibration was performed with the gel filtration

calibration kit (Cytiva) containing 6 proteins in the 13.7-440 kDa range. Chromatograms were analyzed using a set of Gaussian functions.

Spectroscopic characterization

UV-Visible spectra were recorded in a CARY 3500 (Agilent). Circular dichroism (CD) spectra were acquired in a thermostated Chirascan (Applied Photophysics Ltd.) at 25 °C in 50 mM potassium phosphate buffer, pH 7.4 (150 mM ionic strength) in the absence and presence of a 100-fold molar excess of NADH. Near-UV/Vis CD spectra were collected using 20 μM $AIF_{□101}$ in a 1 cm-pathlength cuvette, while Far-UV CD spectra were acquired using 5 μM $AIF_{□101}$ in a 0.1 cm-pathlength cuvette. Fluorescence spectra were acquired in a thermostated Cary Eclipse Fluorescence spectrophotometer (Agilent) using 2 μM $AIF_{Δ101}$ in a 1cm-pathlength cuvette. Flavin fluorescence emission spectra were acquired in the 480-600 nm range upon excitation at 450 nm. Emission spectra of aromatic residues were collected from 300 to 600 nm upon excitation at 280 nm.

Thermal denaturation assays

Thermal denaturation curves were monitored by FAD fluorescence emission, near-UV/Vis CD and far UV-CD. Curves were monitored from 15 °C to 90 °C with scan rates of 1 ºC/min and 1.5 ºC/min respectively for fluorescence and CD assays, both in the presence or absence of a 100-fold excess of NADH. For flavin fluorescence, measures were carried out with 2 μM $AIF_{Δ101}$ in a 1 cm-pathlength cuvette with

excitation at 450 nm. For far-UV and near-UV/Vis, curves were monitored with 5 μM $AIF_{\Delta 101}$ in a 0.1 cm-pathlength cuvette or 20 μM $AIF_{\Delta 101}$ in a 1 cm-pathlength cuvette, respectively. Experimental data were roughly normalized to values between 0 and 1 and globally fitted to a two-step (native (N) ↔ unfolded (U)) or three-step unfolding model (native (N) ↔ intermediate (I) ↔ unfolded (U)) using the following equations [43]:

$$S_{obs} = \frac{S_N + m_N T + (S_U + m_U T) e^{-(\Delta G/RT)}}{1 + e^{-(\Delta G/RT)}} \qquad \text{Eq. 1}$$

$$S_{obs} = \frac{S_N + m_N T + (S_I + m_I T) e^{-(\Delta G_1/RT)} + (S_U + m_U T) e^{-((\Delta G_1 + \Delta G_2)/RT)}}{1 + e^{-(\Delta G_1/RT)} + e^{-((\Delta G_1 + \Delta G_2)/RT)}} \quad \text{Eq. 2}$$

in which S_{obs} is the measured protein signal at a given temperature (T), S_x (S_N, S_I and S_U) represents the y-intercept of native, intermediate and unfolded protein at 0K and m_x (m_N, m_I and m_U) is the slope of the native, intermediate and unfolded states, respectively. The Stabilization Gibbs energy depends on temperature according to $\Delta G = \Delta H\left(1 - \frac{1}{T_m}\right) + \Delta C_P \left(T - T_m - T \ln \frac{T}{T_m}\right)$, where ΔH is the unfolding enthalpy, T_m is the midtransition temperature, ΔC_P is the unfolding heat capacity change, and R is the ideal gas constant.

Kinetic measurements

The steady-state diaphorase activity of $AIF_{\Delta 101}$ was measured in a Cary 100 spectrophotometer (Agilent). The measurements were carried out in air saturated 50 mM potassium phosphate buffer, pH 7.4 at 25 °C, using NADH or NADPH as the substrate donor and 95 μM

dichlorophenolindophenol (DCPIP, $\Delta\varepsilon_{620nm}$= 21 mM^{-1} cm^{-1}) as acceptor [20]. Initial reaction rates at different NADH concentrations were fitted to the Michaelis-Menten equation to determine the kinetic constants:

$$\frac{\nu}{e} = \frac{k_{cat}\,[NAD(P)H]}{K_m^{NADH} + [NAD(P)H]} \quad \text{Eq. 3}$$

$$\frac{\nu}{e} = \frac{k_{cat}/K_m^{NAD(P)H}\,[NAD(P)H]}{1+\frac{k_{cat}/K_m^{NAD(P)H}\,[NAD(P)H]}{k_{cat}}} \quad \text{Eq. 4}$$

In which ν represents the initial velocity, e is the enzyme concentration, $K_m^{NAD(P)H}$ stands for the Michaelis constant for the NAD(P)H, k_{cat} is the turnover number of the enzyme and $k_{cat}/K_m^{NAD(P)H}$ is the enzyme catalytic efficiency.

The reactivity of the CTC towards molecular oxygen was examined by full reduction of $AIF_{\Delta 101}$ with NADH (1:1.5 ratio relative to $AIF_{\Delta 101}$), in both presence or absence of CHCHD4 (1:3 ratio relative to AIF) in 50 mM potassium phosphate buffer, pH 7.4 and 25 ºC as previously reported[41]. Reoxidation was monitored using a Cary 100 spectrophotometer (Agilent).

A SX18.MV stopped-flow spectrophotometer (Applied Photophysics Ltd.) was used to investigate the reductive half-reaction of $AIF_{\Delta 101}$ variants upon mixing with increasing concentrations of NADH (0.03-10 mM) in both the absence and presence of CHCHD4 (1:3 ratio with respect to AIF). Measurements were collected using PDA and monochromator detectors in air-saturated 50 mM potassium phosphate buffer, pH 7.4, at 25 °C. Observed rate constants (k_{obs}) for HT were determined by global fitting of the spectra or exponential fitting of

single-wavelength traces, assuming a one-step process using Pro-K and ProData-XD software. The averaged k_{obs} at each NADH concentration were then non-linearly fitted to the equation that describes the formation of an enzyme:substrate complex prior to the HT event:

$$k_{obs} = \frac{k_{HT}NADH}{K_d^{NADH} + NADH} + k_{rev} \qquad \text{Eq.4}$$

In which k_{HT} and k_{rev} represent the HT constant and its reverse reaction, respectively and K_d^{NADH} stands for the dissociation constant of the transient $AlF_{\Delta 101}$:NADH complex.

Isothermal titration calorimetry (ITC)

ITC assays were performed using an Auto-iTC200 (Malvern) thermostated at 25 ºC for nuclease Cyclophilin A (CypA), 15ºC for dsDNA or 10 ºC for CHCHD4. Typically, 100 µM CHCHD4, CypA or dsDNA were used to titrate ~10 µM $AlF_{\Delta 101}$. Solutions were degassed at 15 °C for 3 min before each assay. A sequence of 2 µL injections of titrant solution every 150 s was programmed, and the stirring speed was set to 750 rpm. The association constant (K_a), the enthalpy of binding (ΔH), and the binding stoichiometry (N) were estimated through non-linear least-squares regression of the experimental data using a single ligand binding site model implemented in Origin 7.0 (OriginLab). The dissociation constant (K_d), the free energy change (ΔG), and the entropy change (ΔS) were calculated from basic thermodynamic relationships.

Electrophoretic-mobility-shift-assays (EMSAs)

DNA retardation assays were carried out as formerly described [36]. Briefly, 500 ng of GeneRuler 100 bp dsDNA ladder (Thermo Scientific) were incubated with 6 µg of $AIF_{\Delta 101}$ for 30 min at 25 °C in 50 mM potassium phosphate buffer, pH 7.4 and subsequently mixed with 6x DNA loading dye (Thermo Fisher Scientific. The samples were resolved by electrophoresis in 1% agarose gel stained with SYBR™ Safe. The electrophoresis was carried out for 1h at 90 V.

Nuclease activity assays

Assays were performed as previously described [36]. Briefly, 250 ng of a double-stranded supercoiled pcDNA3.1 plasmid were incubated at 30 ºC with 250 ng of purified $AIF_{\Delta 101}$ for 1 or 5 minutes in 20 mM Tris, pH 8.0 supplemented with 0.1 mM $CaCl_2$ and 1 mM $MgCl_2$. The samples were subsequently mixed with 6x DNA loading dye (Thermo Fisher Scientific), heated for 10 minutes at 65 °C, and loaded onto a 0.7% agarose gel with SYBR™ Safe. The electrophoresis was carried out for 1 h at 90 V.

Crystallization and structure determination of the $E336K_{\Delta 101}$ variant

Crystallization was carried out using hanging-drop vapor diffusion at 20 °C, mixing $E336K_{\Delta 101ox}$ protein solution (10 mg/ml) with reservoir solution (18% PEG 6K, 0.1 M Tris-HCl pH 8.5, 0.2 M Li_2SO_4) [20]. Crystals were cryoprotected with 20% glycerol and flash-cooled in liquid

nitrogen. X-ray diffraction data were collected at 100 K on the BL13-XALOC beamline (ALBA Synchrotron) using a Pilatus3 X 6M detector. Data were processed with XDS [28] and SCALA [16] from the CCP4 package [55], and the structure was solved by molecular replacement using Phaser [30], with $AIF_{\Delta 101ox}$ (PDB 4BV6) as the search model. Model building and refinement used Coot [15], phenix.refine [3], and REFMAC [34], yielding a final model containing residues 127–610, one FAD molecule, one glycerol, and 239 water molecules. Residues 546-558 and the last three C-terminal residues were unresolved. Data collection and refinement statistics are provided in Table S3.

Data and statistical analysis

Data were analyzed and shown using StatView 5.0 (SAA Institute, Mesa, AZ, USA), SigmaPlot (Systat. Software Inc.), Origin 7.0 (OriginLab) and Pro-K (Applied Photophysics Ltd.) and PyMol [11]. Results were displayed as mean ± SD and statistically analyzed using either the Mann-Whitney U test when comparisons between two groups were performed, or the Bonferroni correction, for multiple comparisons. Differences were considered statistically significant at $p \leq 0.05$ for Mann-Whitney U test or $p \leq 0.0167$ for Bonferroni correction.

Results

Clinical findings

Patients and Clinical Evaluation

We report the case of a 64-year-old male from Aragón, Spain, with a progressive sensorimotor polyneuropathy. Genetic testing confirmed a diagnosis of X-linked hereditary sensorimotor polyneuropathy (CMTX4/COWCK), associated with a hemizygous mutation c.1006G>A (p. Glu336Lys) in the *AIFM1* gene (Xq26.1). Family history revealed that his mother and daughter are carriers of the same mutation, and his brother is also affected.

Natural History and Clinical Progression

The patient was born in 1961. Since childhood, he exhibited hypotonia, generalized areflexia, and pes cavus, for which he underwent orthopaedic surgery at the age of 8. He also developed progressive bilateral sensorineural hearing loss, requiring hearing aids by age 25. By age 41, hearing loss reached 90% bilaterally. A right cochlear implant (Nucleus 7) was placed at age 57 with partial benefit. He underwent cataract surgery at age 38.

Motor disability followed a slowly progressive course. At the age of 32, he discontinued playing tennis due to fatigue and weakness in the lower limbs. At 38, he required unilateral walking support. He was evaluated at the neuromuscular unit of Hospital Universitario Miguel Servet at the age of 41 (in 2003). Severe gait ataxia was documented. Neurological exam showed visual acuity of 0.8 bilaterally, global weakness graded 4/5 in the upper limbs and pelvic girdle, and 1-2/5 in foot flexors/extensors, with marked distal amyotrophy producing a "stork leg" appearance and post-surgical clubfoot. He had global

areflexia, preserved thermal sensitivity, and reduced tactile and pain sensation in a glove-and-stocking pattern. Joint position and vibration senses were abolished in the lower limbs and decreased distally in the upper limbs. Mild finger-to-nose ataxia was present; lower limb ataxia was severe and disabling. There was no truncal ataxia. Cardiovascular exam was normal. Associated symptoms included oscillopsia and nystagmus diagnosed by ophthalmology.

Metabolic testing was normal. Brain Magnetic Resonance Imaging (MRI) and cardiological evaluation were unremarkable. A heterozygous GAA repeat expansion (250 repeats) in FRDA/X25 led to a provisional diagnosis of Friedreich's ataxia. As compound heterozygosity was suspected, further studies were initiated.

By age 45 (2007), he needed a wheelchair for distances >50 meters. Manual dexterity declined significantly, affecting eating and typing. He required assistance with all activities of daily living (ADLs). Arm strength was preserved (5/5), though clumsy fine motor control was noted. Pansensory hypoesthesia was present in the lower limbs and reduced sensation in arms.

In 2009, FRDA repeat expansion testing was repeated, excluding Friedreich’s ataxia. GDAP1 testing (2010) was negative for pathogenic variants.

At age 55 (2016), genetic revaluation revealed a hemizygous c.1006G>A (p. Glu336Lys) mutation in exon 10 of *AIFM1* (NM_004208.4) (Fig. 1A). This change results in the substitution of glutamic acid with lysine at position 336 of the protein (p.Glu336Lys),

generating a missense mutation. This variant has not been reported in population databases (gnomAD v4.1.0, exomeAD). The results of bioinformatics analysis systems for predicting the effect of mutations indicate, in 7 out of 9 prediction tools used (PROVEAN, SIFT, PolyPhen2, LRT, MutationTaster, MutationAssessor, and CONDEL), that this is a deleterious variant. Currently, this variant is reported in the ClinVar database (ID: 641733) as a likely pathogenic variant (SCV000934480.7) and as a variant of uncertain significance (SCV004036880.1, SCV002765018.3). Using ACMG criteria, this variant is classified as likely pathogenic (PP3, PP5, PM1, PM2) [39]. This new mutation confirmed Cowchock syndrome, being the clinical status of the patient stable but severely disabled. The patient was wheelchair-bound, with severe impairments in fine motor skills, worsened by deafness and oscillopsia. Occasional choking episodes with aspiration and self-limited vestibular symptoms were reported. He developed muscle contractures that were refractory to all muscle relaxants and showed a fluctuating course. Repeated brain MRI and vestibulocochlear nerve imaging were unremarkable. Visual evoked potentials revealed a delayed P100 latency at 153 ms, while brainstem auditory evoked potentials were bilaterally absent.

In 2017, the patient continued to exhibit profound motor and sensory impairment, with complete dependence in ADLs except for feeding. Communication was limited to lip-reading. Riboflavin therapy was maintained.

By 2019, the cochlear implant was functioning effectively. The patient remained physically stable, ambulating short distances with bilateral support and driving long distances. Manual dexterity was slower but preserved. Muscle strength was graded 5/5 in the upper limbs and approximately 4+/5 in the hands. Distal tactile, vibratory, and proprioceptive hypoesthesia persisted, without evidence of clinical progression.

He reported mood instability characterized by depressive and irritable episodes, as well as sleep disturbances. Riboflavin was reduced to 50 mg twice daily due to gastrointestinal intolerance.

Family genetic studies confirmed that his mother, and daughter were carriers of the *AIFM1* variant. His brother was also clinically affected, with a phenotype consistent with polyneuropathy.

Annual follow-ups from 2021 to 2024 documented persistent chronic shoulder pain interfering with sleep, together with a slow progression of motor and sensory deficits. Manual skills gradually declined, with frequent dropping of objects and difficulty fastening buttons. At home, he ambulated with a cane and demonstrated brachial strength of 4+ distally and 5/5 proximally. Distal sensory loss remained evident, with absent deep tendon reflexes (0/4). Cognitive function was preserved, and mood remained stable.

A graphical timeline showing the progression of the patient’s disability is presented in (Fig. 1B).

The following complementary studies were carried out to aid in the phenotypic characterization of the patient: i) Neurophysiological

evaluation (EMG/NCS) demonstrated a severe, length-dependent, axonal sensorimotor polyneuropathy without signs of active denervation. ii) Sensory nerve conduction studies revealed absent responses in the sural and superficial peroneal nerves bilaterally, and reduced amplitudes with delayed latencies in the median and ulnar nerves, consistent with moderate sensory neuropathy. iii) Motor conduction studies showed absent responses in the common peroneal and tibial nerves bilaterally, and reduced amplitudes with mild to moderate slowing in the median and ulnar nerves. iv) Electromyographic examination revealed mixed recruitment patterns without spontaneous activity. The detailed findings of the study are summarized in Tables 2 and 3. These results are consistent with a severe axonal sensorimotor neuropathy, supporting the clinical diagnosis of Charcot-Marie-Tooth disease type X4 (CMTX4, Cowchock syndrome), subsequently confirmed by genetic testing of the *AIFM1* mutation.

Impact of the E336K mutation on OXPHOS performance

To investigate the impact of the E336K mutation on AIF cellular functions, fibroblast-like cell lines were established from skin biopsies of the affected individual and a healthy control and subsequently immortalized. Prior to their use as a disease model, the phenotype of immortalized fibroblasts was compared with that of the corresponding primary cell lines with respect to the two roles of AIF within mitochondria: growth capacity in galactose-containing medium (as an

indicator of its role in energy metabolism) and susceptibility to parthanatos induction. As shown in Fig. S1, the immortalized cells exhibited a behavior comparable to that of the primary cells in both assays, supporting their suitability as a reliable disease model for the present study.

To analyze whether the mutation alters transcriptional regulation or protein stability, AIF expression was assessed at the mRNA and protein levels using quantitative RT-PCR and Western blot analysis, respectively. As shown in Fig. 2A and 2B, although the relative expression levels of AIF mRNA in mutant fibroblasts were comparable to those of control cells, the amount of AIF protein was significantly reduced, suggesting decreased stability of the mutant protein. Given AIF's role in mitochondrial biogenesis and function, we next analyzed the impact of the mutation on OXPHOS performance. Mutant fibroblasts exhibited significantly impaired growth when cultured in galactose medium compared to glucose (Fig. 2C), indicating defective OXPHOS capacity. This impairment was confirmed by direct measurements of oxygen consumption in intact cells, which revealed an average ~50% reduction in basal respiration compared to controls (Fig. 2D). Results of cell growth sensitivity to different inhibitors of respiratory complexes (Fig. S2A) suggested that this reduction might be mainly due to defects in mitochondrial complexes I and III function as mutant cells displayed significantly more sensitivity than control cells to rotenone and antimycin A, specific inhibitors of these complexes. To further investigate this, the structural organization of mitochondrial

respiratory complexes and supercomplexes (SCs) as well as the enzymatic activities of the respiratory complexes were analyzed by native electrophoresis followed by WB (Fig. 2E) and spectrophotometry (Fig. 2F), respectively. Analysis of the SCs pattern revealed an overall decrease in the levels of assembled respiratory complexes and SCs in mutant cells, normalized to CII, with a more pronounced reduction observed for SCs (to around 30-40 % compared to the control (mean of 2 biological replicates)). As shown in Fig. 2E, mutant cells exhibit reduced incorporation of CIII and CIV into their corresponding SCs accompanied by a relative accumulation of their free dimeric ($CIII_2$) or monomeric (CIV) forms. Accordingly, the $CIII_2$/CIII-SCs ratio increased from 0.4 in control cells to 0.8 in mutant cells, while the CIV/CIV-SCs ratio increased from 1.9 to 2.8, respectively. These findings are consistent with impaired respirasome formation or stability, possibly associated with reduced levels of CI or CIII. In agreement with this, spectrophotometric assessment of OXPHOS complex activities showed a significant decrease in the combined activities of complexes I+III and II+III (Fig. 2F) while no change was detected for complex I.

To better understand the molecular basis for mitochondrial dysfunction and disease associated with the E336K mutation in AIF, we assessed the expression of CHCHD4 -the physiological mitochondrial inner membrane partner of AIF [22, 38]- both at the mRNA and protein levels. The mutation of AIF negatively affects CHCHD4 mRNA and protein expression, as its relative levels were significantly reduced compared to those of control cells (Fig. 3A and 3B). In line with these observations,

mitochondrial content levels, evaluated both by MitoTracker™ Green staining followed by flow cytometry and mtDNA copy number quantification (Fig. 3C) were significantly reduced in E336K cells. To further investigate the effects of this impairment on the biogenesis of the OXPHOS system, the steady-state levels of mitochondrial respiratory complex subunits were quantified on whole cell extracts, showing a decrease of the relative levels of complexes I, III and IV subunits in mutant cells when compared to those of control fibroblasts (Fig. 3D). Thus, while the levels of complex I subunits normalized to actin were significantly reduced to approximately 70% of those observed in control cells, the signals of UQCRC1 (Ubiquinol-Cytochrome C Reductase Core Protein 1, CIII) and MT-CO1 (CIV) decreased to about 50% of control cells in both cases. In contrast, the levels of SDHA, a CII subunit, were slightly but significantly higher than those observed in control cells.

Finally, we investigated whether these alterations affect mitochondrial ROS production, which could potentially affect the disease phenotype. As illustrated in Fig. 4A, the production of mitochondrial superoxide, quantified by flow cytometry following cell staining with MitoSOX, was significantly lower in mutant cells compared to controls. Although this observation seems to contradict with the mitochondrial dysfunction, this difference was abolished when ROS levels were normalized to mitochondrial content (Fig. 4B). Moreover, mitochondrial superoxide dismutase (SOD2) mRNA expression was significantly decreased in mutant cells (Fig. S2B), indicating that the reduced ROS signal is not

due to compensatory upregulation of mitochondrial antioxidant defenses.

In summary, the E336K mutation reduces AIF protein stability, impairs OXPHOS capacity through defective assembly of respiratory supercomplexes, decreases CHCHD4 expression, and lowers mitochondrial content, altogether leading to compromised mitochondrial function.

The E336K mutation alters redox properties, conformational dynamics, and CHCHD4 interaction in AIF

To better understand the molecular basis of the pathogenicity associated with the E336K substitution identified here, we further characterized the recombinant mutant protein using the synthetic constructs E336K$_{\Delta 77}$ and E336K$_{\Delta 101}$. These constructs correspond, respectively, to the soluble moiety of the mitochondrial form of AIF lacking the 24-residue transmembrane segment and to a truncated form mimicking the apoptogenic AIF isoform [20, 52]. The corresponding WT$_{\Delta 77}$ and WT$_{\Delta 101}$ proteins were analyzed in parallel as appropriate controls. Both mutant isoforms were purified to homogeneity, but with markedly different outcomes. E336K$_{\Delta 101}$ exhibited a UV-visible absorption spectrum comparable to that of the WT$_{\Delta 101}$ protein, displaying the characteristic flavin bands I and II at 451 and 380 nm, respectively, along with a shoulder at 467 nm (Fig. S3A). These features indicate that the flavin cofactor remained in the oxidized state and was properly incorporated into the protein. In

contrast, protein form E336K$_{\Delta 77}$ progressively lost the flavin cofactor during purification and handling, ultimately showing a strong tendency to precipitate. These observations indicate *in vitro* protein instability that may be consistent with the reduced protein levels of the mitochondrial isoform detected in patient-derived fibroblasts. Due to the low purification yield and the reduced ability of the mitochondrial E336K$_{\Delta 77}$ isoform to retain the FAD cofactor, subsequent analyses focused on the apoptotic E336K$_{\Delta 101}$ variant.

This mutant oxidized form, E336K$_{\Delta 101ox}$, displayed an apparent molecular weight (appMW) of ~52 kDa, consistent with a monomeric state as determined by size exclusion chromatography (Fig. 5A and 5C). Additionally, its CD spectral properties were comparable to those of WT, indicating that the mutation does not affect overall protein folding (Fig. S3B). In contrast, the mutant's NADH reduced form, E336K$_{\Delta 101rd}$, showed significant alterations in its spectroscopic properties, including changes in the shape of the far-CD signals and attenuation of the fluorescence quantum yield of at least one tryptophan (Fig. S3 B-D). Moreover, upon NADH incubation, the mutant protein eluted as three peaks with appMW values of ~150, ~128 and ~65 kDa (Fig. 5B and 5D), corresponding to a dimeric form, a dimer-monomer transition due to partial reoxidation, and a monomeric form, respectively [20]. These results indicate that the E336K$_{\Delta 101}$ mutant retains its ability to form dimers under reducing conditions, although the dimers exhibit diminished stability and a slightly less compact dimeric assembly compared to the WT protein.

To explore the effects of the E336K mutation on AIF conformational stability, we determined the thermal stability of this mutant protein by monitoring far UV- and near UV-CD as well as flavin fluorescence, in the presence and absence of NADH (Table S4, Fig. S3E-F). The results indicate that the mutation negatively impacts the thermal stability of $AIF_{\Delta 101ox}$ and destabilizes the cofactor environment (Fig. S3E, Table S4), as evidenced by a decrease of ~5-6 degrees in both T_ms values associated with the unfolding process when compared with $WT_{\Delta 101ox}$, while the unfolding mechanism remained unchanged. This destabilizing effect of the E336K substitution likely reflects an intrinsic property of the mutant protein and is consistent with the impaired retention and low stability of the mitochondrial $E336K_{\Delta 77}$ isoform, which precluded its direct analysis. However, when the thermal stability of E336K in the presence of NADH was evaluated, the coenzyme did not destabilize the mutant, in stark contrast to the WT behavior, being the two identified T_ms values being close to those of $E336K_{ox}$ and of NADH reduced $WT_{\Delta 101}$. Altogether, these findings suggest structural and dynamic differences between the WT and the E336K mutant, both in the absence of the coenzyme as well as upon its binding and flavin reduction. In view of these observations, we also investigated the impact of this mutation on AIF redox properties using different biochemical approaches. $E336K_{\Delta 101}$ exhibited a strong decrease in coenzyme affinity regarding $WT_{\Delta 101}$, with a K_m^{NADH} value ~6-fold higher than that of $WT_{\Delta 101}$ (Table 4 and Fig. S4A). In contrast, the turnover number (k_{cat}) remained similar, resulting in a ~3-fold reduction in

catalytic efficiency relative to $WT_{\Delta 101}$. Notably, the mutant displayed both a ~2-fold higher turnover number and a ~23-fold greater affinity for NADPH compared with $WT_{\Delta 101}$ to NADH (Table 4 and Fig. S4B). Consequently, the $E336K_{\Delta 101}$ variant was substantially more efficient at oxidizing NADPH than the WT protein, with an estimated ~1000-fold increase in the k_{cat}/K_m^{NADPH}, thereby markedly reducing the specificity for NADH over NADPH compared to the $WT_{\Delta 101}$.

To assess the mutation impact on HT from the NADH coenzyme to the FAD cofactor, we performed stopped-flow transient analysis (Table 4 and Fig. S4C). In $E336K_{\Delta 101}$, as in $WT_{\Delta 101}$, the complete FAD reduction was accompanied by a progressive formation of isoalloxazine:NAD^+ CTC, with similar spectral intensity, suggesting a comparable extent of CTC stabilization (Fig. 5E-F). However, unlike the native protein –where the CTC had a half-life of 20 minutes– $E336K_{\Delta 101}$ did not reach full reduction at stoichiometric molar coenzyme concentrations. This incomplete reduction impeded CTC stabilization and precluded assessment of its reactivity towards O_2. Furthermore, the mutant exhibited faster HT (~2-fold increase) and lower coenzyme affinity (~2-fold decrease), while maintaining similar HT efficiency (Table 4). These results demonstrate that the E336K mutation significantly compromises the redox properties of AIF by decreasing NADH binding affinity and destabilizing the CTC.

Considering previous findings and the relevance of AIF dimer stabilization for the formation of a long-lived complex with CHCHD4 [9, 22, 42], we investigated the impact of the mutation on this interaction

using ITC (Fig. 5G and Table S5). As previously reported for $WT_{\Delta 101ox}$ [41], no heat exchange was detected when titrating $E336K_{\Delta 101ox}$ with CHCHD4, indicating a lack of specific binding under the assayed conditions. In the presence of NADH, the $E336K_{\Delta 101rd}$ mutant was able to bind CHCHD4, but with slightly lower affinity than $WT_{\Delta 101rd}$ (K_d ~ 5-fold higher than for $WT_{\Delta 101rd}$:CHCHD4 complex) and with notable differences in thermodynamic contributions to the binding. The $WT_{\Delta 101rd}$:CHCHD4 interaction was mainly driven by a strong favorable enthalpic contribution, typical of specific binding, while the entropic term was unfavorable. In contrast, the $E336K\Delta_{101rd}$:CHCHD4 complex showed a weaker enthalpic contribution and even a favorable entropic term, suggesting that non-specific forces may play a more prominent role. This altered thermodynamic profile could impair the formation of a functional $E336K_{\Delta 101rd}$:CHCHD4 complex, which is crucial for mitochondrial homeostasis [9, 22].

Impact of E336K mutation on AIF structure

To investigate the structural impact of the E336K mutation, the X-ray crystal structure of $E336K_{\Delta 101ox}$ was resolved and evaluated in the context of structures for monomeric $WT_{\Delta 101ox}$ and dimeric $WT_{\Delta 101rd}$:NAD^+ [20] (Fig. 6A). Superposition of $WT_{\Delta 101ox}$ and $E336K_{\Delta 101ox}$ revealed a high degree of structural similarity (r.m.s.d. = 0.21 Å for 451 atoms), with both structures a sharing similar overall fold. Comparison with $WT_{\Delta 101rd}$: NAD^+ (r.m.s.d. = 1.06 Å for 400 atoms) showed that the conformational rearrangements of the β-hairpin and regulatory C-loop associated with coenzyme binding were absent in $E336K_{ox}$. This

suggests that the E336K substitution, in agreement with the monomeric conformation observed by size exclusion chromatography, does not promote permissive dimer formation as reported for other AIF variants [8].

In $WT_{\Delta 101ox}$ and $WT_{\Delta 101rd}$:NAD^+ structures, the side chain of E336 adopts a similar orientation (Fig. 6B). Notably, in the $WT_{\Delta 101rd}$:NAD^+ structure, the E336 carboxylate oxygen atoms (O2B and O3B) hydrogen bond to the hydroxyl groups of the ribityl moiety of the adenine nucleotide portion of NAD^+ (sitting at 2.8 and 3.5 Å respectively) [20]. Substitution of E336 with lysine may disrupt this interaction, as the positively charged and longer lysine side chain might preclude an orientation conducive to coenzyme hydrogen bonding (Fig. 6B). Furthermore, as shown in Fig. 6C, the mutation modifies the electrostatic landscape of the environment surrounding residue 336, particularly in the cleft where the ribose of the adenine nucleotide moiety of the coenzyme binds. This surface becomes more positive and potentially eager to accommodate the 2'-phosphorylated ribose form of the coenzyme, NADPH. This is exemplified in Fig. 6D, where based on the $WT_{\Delta 101rd}$:NAD^+ structure a model for the $E336K_{\Delta 101rd}$:$NADP^+$ interaction is presented, envisaging the interaction between the 2′-P of NADPH and residues K336 and K342. Such differences in surface charge distribution between the WT and the mutant may correlate with the observed stability and enzymatic activity alterations and are particularly in line with the E336K preference for using NADPH as a hydride donor (Table 4).

Impact of the E336K mutation on AIF-mediated cell death and nuclear interactions

As mentioned, besides its role in mitochondrial function and biogenesis, AIF also participates in a caspase-independent cell death pathway known as parthanatos [47]. To analyze whether the E336K variant alters this function, control and mutant fibroblasts were exposed to the alkylating agent MNNG for 20 minutes to induce cell death. After 24 hours, cell death was quantified by flow cytometry using annexin V-FITC and 7-AAD staining. As shown in Fig. 7A, both control and mutant cells underwent cell death; however, the percentage of dead cells was significantly lower in cultures expressing the E336K mutant (Fig. 7B). Consistently, MTT assays revealed greater growth inhibition in mutant cells compared to controls, with viabilities of 22% and 45.9%, respectively. These results indicate that although the E336K mutation does not abolish AIF-mediated cell death, its efficiency in fibroblasts appears reduced (Fig. S2C).

Upon apoptotic stimuli, AIF translocates from the mitochondria to the nucleus, where it is proposed to form a DNA-degradosome complex – through interactions with proteins such as the endonuclease CypA– essential for the caspase-independent apoptotic pathway [5, 36]. To assess the impact of the E336K mutation on AIF's interactions with its nuclear partners, we performed *in vitro* ITC using dsDNA and CypA as ligands and recombinant $WT_{\Delta 101}$ and $E336K_{\Delta 101}$ proteins (Fig. 7C, Fig. S5C-F and Table S5). Both $WT_{\Delta 101}$ and $E336K_{\Delta 101}$ proteins exhibited similar binding affinities toward dsDNA and CypA, with K_d in the

micromolar range for both interactions. The thermodynamic profiles of the interactions with dsDNA were also comparable between variants and predominantly entropy-driven, consistent with non-specific electrostatic interactions previously described for WT AIF. EMSA further confirmed similar DNA-binding behavior, with both variants exhibiting comparable levels of DNA retention in the gels (Fig. 7D). These results suggest that the E336K mutation does not significantly affect the intrinsic ability of AIF to bind DNA.

Notably, some differences were observed in the interaction with CypA. $WT_{\Delta 101}$ exhibited a strong enthalpy-driven interaction with a modest positive entropy change, indicative of a specific well-defined binding interface [18, 19, 36]. In contrast, the pathological variant showed a slightly weaker enthalpic contribution (Fig. 7C and Table S5), potentially reflecting minor conformational rearrangements upon complex formation.

Given the recently reported intrinsic nuclease activity of AIF [36], we investigated the impact of the E336K mutation on AIF-mediated DNA degradation. The E336K mutation does not suppress the intrinsic DNA-cleaving capability of AIF when using purified plasmid DNA as substrate, exhibiting an activity comparable to that of the WT protein (Fig. 7E).

In summary, these findings demonstrate that the E336K mutation does not abolish the intrinsic capacity of AIF to interact *in vitro* with DNA and CypA, although it subtly alters the thermodynamics of CypA binding

and may modestly reduce the efficiency of parthanatos induction in patient-derived fibroblasts.

Discussion

This study provides the first integrated clinical, cellular and molecular mechanistic characterization of the novel pathogenic *AIFM1* variant E336K. This combined approach significantly broadens the mechanistic and phenotypic spectrum of AIF-related disease. Our data strongly suggest that the pathological impact of E336K is primarily driven by loss of AIF's pro-survival, mitochondria-supporting, function rather than by impairment of its pro-death role [6, 47, 56]. Clinically, the patient presented with progressive axonal sensorimotor neuropathy and sensorineural hearing loss, while cognition remained preserved –a phenotype consistent with CMTX4/Cowchock syndrome and well within the established spectrum of *AIFM1*–related disorders. These findings underscore both the diagnostic challenges associated with *AIFM1* mutations and the importance of variant-specific functional analyses to refine genotype–phenotype correlations [6, 46, 56].

At the cellular level, patient-derived fibroblasts displayed reduced AIF protein, impaired OXPHOS capacity, and defective organization of respiratory supercomplexes, which were not accompanied by an increase in mitochondrial superoxide production. Notably, CHCHD4 expression and mitochondrial content were decreased, coherently

linking the cellular phenotype to the AIF–CHCHD4 axis, which is known to support the import, oxidative folding, and assembly of specific respiratory components [9, 17, 22, 38, 42]. The reduction in mitochondrial content together with the lower respiratory flux in mutant cells may explain the apparently counterintuitive decrease in mitochondrial ROS at baseline. Moreover, remodeling of SCs organization may alter electron leak probability without necessarily increasing net mitochondrial superoxide levels. Taken together, our findings suggest a model in which mitochondrial remodeling and reduced respiratory activity may contribute to the lower steady-state mitochondrial superoxide levels observed, rather than necessarily reflecting improved redox homeostasis.

Crystallographic analysis provides a structural rationale: substitution of Glu336 with Lys remodels the electrostatic potential of the coenzyme binding pocket, precisely at the site of the adenosine-ribose moiety of NADH –a key region for stabilizing the CTC and mediating redox-driven conformational changes in AIF [20, 46]. In parallel, *in vitro* analyses indicate that the E336K mutation is associated with conformational destabilization and reduced flavin binding stability. Taken together, these structural and biochemical alterations are consistent with a primary disruption of AIF's pro-survival role, potentially compromising its role in mitochondrial maintenance and respiratory chain biogenesis, offering a unifying structural explanation for the patient's biochemical phenotype [8, 20, 46, 52]. Collectively, these alterations may decrease AIF's ability to sense mitochondrial NADH redox state and to sustain

the conformational ensembles that underwrite its pro-survival functions [8, 52].

Of particular relevance are the results of the systematic molecular analysis of AIF's intrinsic interaction network with physiological partners. Mechanistically, the reduced dimeric form of AIF interacts with CHCHD4 to support mitochondrial disulfide relay and respiratory chain assembly [9, 22, 42]. While E336K retained the ability to dimerize, the resulting dimers were less stable and less compact. Moreover, its interaction with CHCHD4 displayed markedly reduced affinity and altered thermodynamic signatures, indicating a weakened and less specific interacting interface. These molecular changes provide a direct link to the observed cellular phenotypes –decreased CHCHD4 levels, reduced mitochondrial content, and disorganized supercomplexes– and offer a cohesive explanation for the OXPHOS insufficiency observed in patient-derived fibroblasts. In contrast, the apoptogenic properties of AIF were largely preserved, with intact intrinsic properties such as DNA binding, CypA interaction and nuclease activity, and only a partial attenuation of parthanatos induction in mutant fibroblasts, possibly reflecting reduced mutant protein stability. This clinical-biological dissociation —characterized by dominant mitochondrial dysfunction despite preserved apoptotic competence— has also been reported for the closely located pathogenic variant M340T and for several additional AIFM1 variants (F210L/S, R422Q, V243L, G308E, G338E), which retain apoptotic activity *in vitro*, including DNA binding and nuclear translocation, while exhibiting

markedly reduced redox function. Together, these observations reinforce the concept that mitochondrial impairment, rather than defective apoptosis, is the primary driver of disease across this subset of the AIFM1 mutational spectrum (Table 1 and S1).

Despite these findings, several limitations of the present study should be acknowledged. To strengthen genotype–phenotype correlations, additional healthy control lines should be analyzed. Moreover, although fibroblasts represent a suitable model to assess the impact of the E336K mutation on AIF function due to the minimally invasive nature of biopsy collection, the phenotypic consequences of the mutation may be more pronounced in cell types with greater dependence on mitochondrial ATP production, such as muscle cells or neurons

From a translational perspective, these findings highlight the need to integrate structure-function studies into the interpretation of *AIFM1* variants, particularly in X-linked neuropathies with hearing loss. Therapeutic strategies based on cofactor supplementation may hold promise, especially in cases with impaired FAD retention and binding stability, as observed in this study. The shift toward NADPH utilization further suggests a possible compensatory route that could be therapeutically leveraged. More broadly, targeting NADH-driven allosteric regulation, stabilizing the CTC, or enhancing the robustness of the CHCHD4 pathway represent concrete, testable avenues for future intervention.

In summary, our work provides a comprehensive clinical-to-molecular characterization of an *AIFM1* mutation. The E336K mutation supports a

recurring principle in *AIFM1*-related disease, whereby alterations affecting NADH-sensing/redox cycle preferentially compromise mitochondrial-supporting functions while leaving intrinsic apoptotic properties relatively intact. Our structural and functional data are consistent with a model in which electrostatic remodeling of the coenzyme-binding site, destabilizing the NADH-dependent CTC, and weakening CHCHD4 engagement may collectively contribute to disease pathogenesis. This framework offers a plausible explanation for the selective vulnerability of high-energy–demand tissues such as peripheral nerves, the inner ear, and muscle. Overall, this study expands the clinical and mechanistic spectrum of *AIFM1* disease, refines the interpretation of *AIFM1* variants, and provides a conceptual basis for future studies exploring mechanism-based therapeutic strategies, including cofactor supplementation and targeted interventions aimed at stabilizing AIF-CHCHD4 function.

Author's contributions

Conceptualization: P.F and R.M-L; Data curation: P.F., R.M.-L., M.M.J., A.V.-C., P.F.-S., M.M and M.B.; Funding acquisition: P.F., R.M.-L, M.M. and P.F.-S.; Investigation: R.M.-L, M.P, R. G-V. and P. F-S (cell culture, respiration and viability analysis), J. M.-B. and C. R-Y (Cytometer measurements), M.F., O.S., M.M.-B. and P.F (protein production and molecular characterization); M.F and M.M.-J (crystallization and structure determination) M.D.M. (genetic analysis) and M.B. (clinical studies). Writing original draft: P.F., R.M.-L., M.F., O.S, M.M-J. and M.B.

Review & editing: all authors. All authors have given approval to final version of the manuscript.

Funding

This work was funded by the Spanish State Research Agency and by FEDER (MCIN/AEI-FEDER, Grants PID2022-136369NB-I00, Grant PID2021-124354NB-I00), as well as by the Gobierno de Aragón, grant number “Grupo de Referencia E35_17R” to M.M-M., M.M, P.F.-S., R.M.-L. and P.F. and grant number “LMP220_21” to P.F.-S. and R.M.-L. The authors would like to acknowledge *Servicios Generales de Apoyo a la Investigación* (SAI), University of Zaragoza, for their support, as well as at BIFI-University of Zaragoza for providing instrumentation.

Data availability

The structural data for the AIF E336K variant generated in this study by X-ray crystallography have been deposited in the Protein Data Bank under accession code PDB 9SZQ.

Declarations

Ethics approval and consent to participate

The study was conducted in accordance with the Declaration of Helsinki. Ethical approval C.P.-C.I. PI18/224 was obtained from Comité de Ética de la Investigación de la Comunidad Autónoma de Aragón (CEICA), Zaragoza, Spain. Written informed consent for participation in this study was obtained from the patient.

Consent for publication

All authors have approved the manuscript.

Competing interests

The authors declare no competing interests

Supplementary information

The only version contains supplementary material available:

Supplementary Figure S1 to Figure S5 and supplementary Table S1 to Table S5.

To submit to Cell Communication and Signaling

Figures

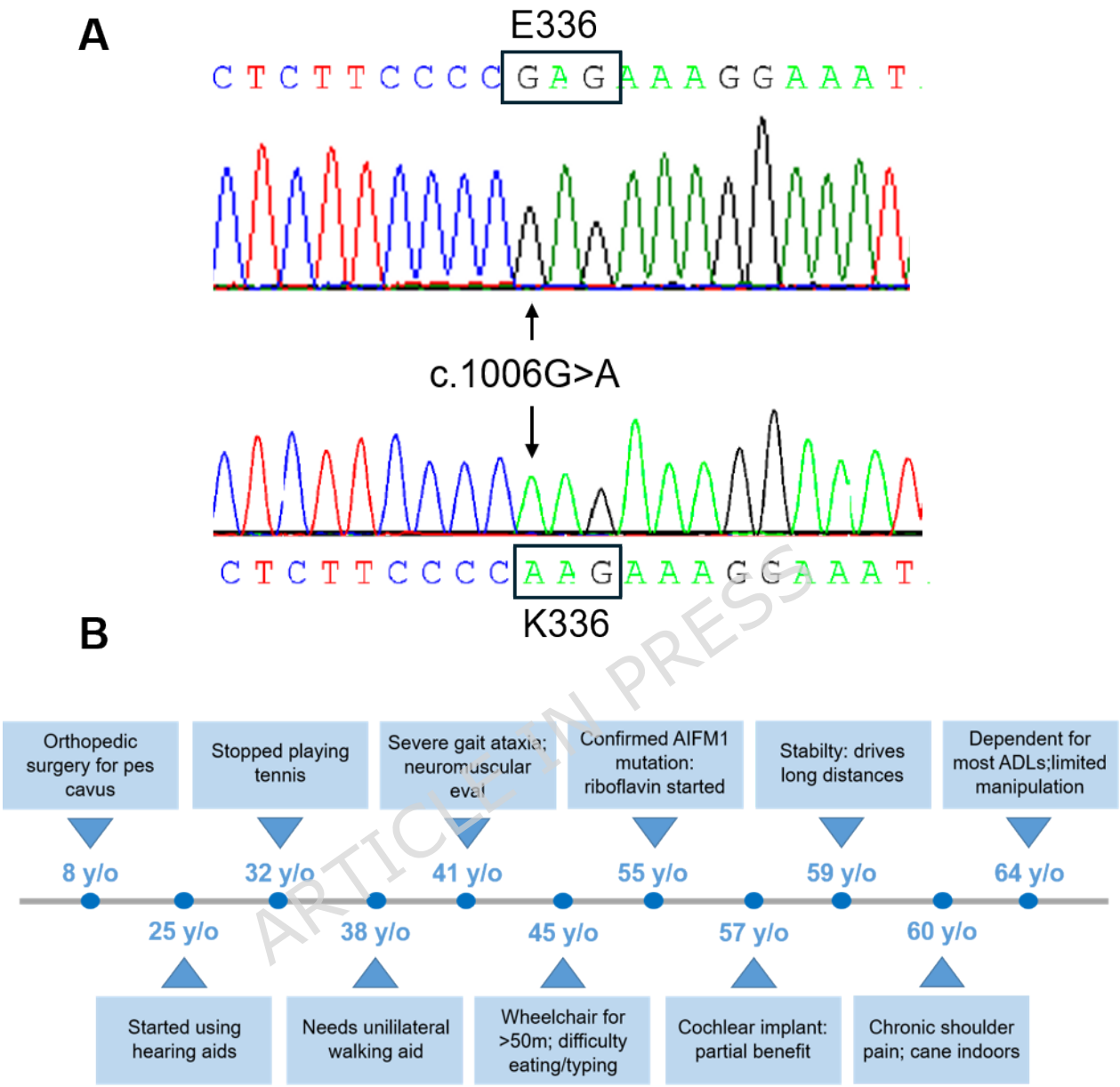

Fig. 1. Genetic confirmation and clinical course of the CMTX4 case. **(A)** Chromatogram showing the m.1006G>A mutation within the *AIFM1* gene in the patient. (**B**) Timeline showing the disability progression in patient with CMTX4. Each symptom is plotted according to the time of

appearance, illustrating the chronological sequence and clinical evolution over the course of the illness.

To submit to Cell Communication and Signaling

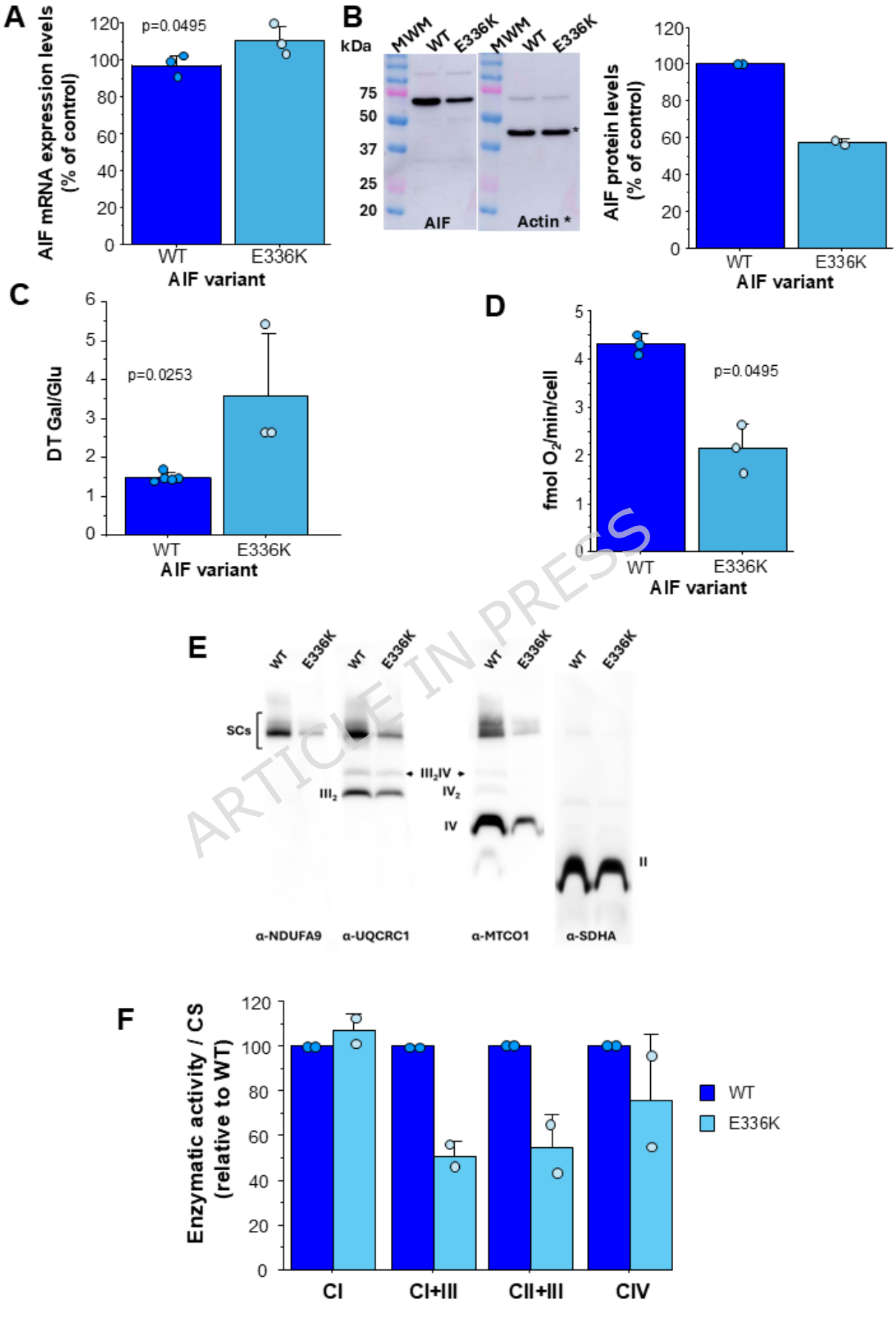

Fig. 2 Effect of the AIF E336K mutation on OXPHOS performance in immortalized fibroblasts. Evaluation of relative expression of AIF at mRNA (**A**) and protein (**B**) levels. (**C)** Doubling time ratio for WT and E336K immortalized fibroblasts in galactose versus glucose containing media. (**D)** Oxygen consumption rate in intact cells for WT and E336K fibroblasts. (**E)** Immunodetection of assembled supercomplexes in digitonin-permeabilized mitochondria from WT and E336K fibroblasts separated by BNGE and probed with specific antibodies for CI (anti-NDUFA9), CIII (anti-UQCRC1), CIV (anti- MT-CO1) and CII (anti-SDHA). **(F)** Spectrophotometric assessment of respiratory complexes enzymatic activities normalized by citrate synthase activity. Data are expressed as mean ± SD of the mean. Sample sizes were as follows: n=3 technical replicates in **(A)**; n=2 biological replicates in **(B)**; n=4 (control) and n=3 (mutant) biological replicates in **(C)**; n=3 biological replicates in **(D)**; and n=2 biological replicates in **(F)** with each one representing the mean of 2-4 technical replicates. Apparent molecular weight of hAIF ~ 57 kDa

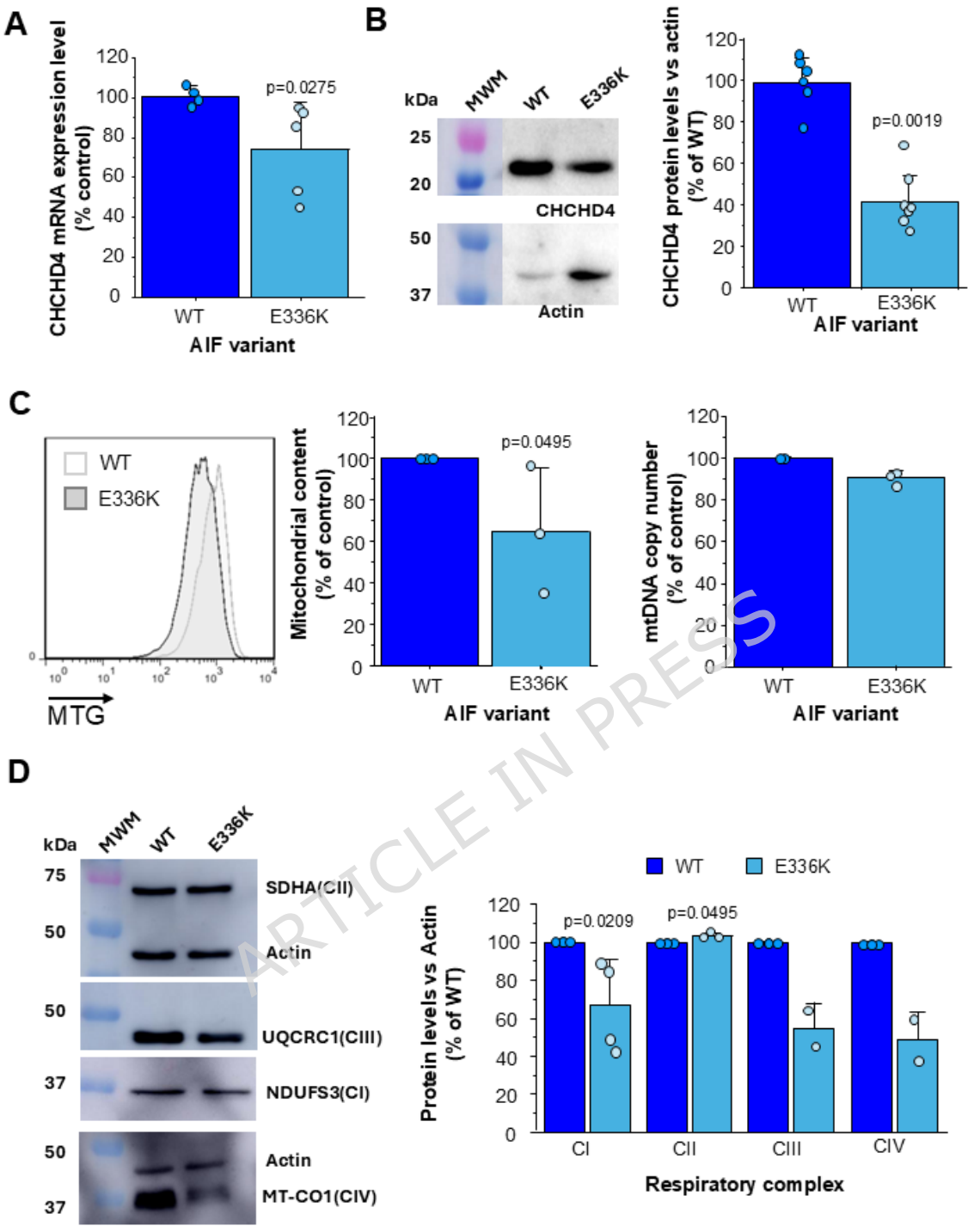

Fig. 3 Impact of the AIF E333K mutation in mitochondrial biogenesis. Measurement of relative expression of CHCHD4 at mRNA (**A**) and protein (**B**) levels in WT and E336K fibroblasts. (**C**) Evaluation of mitochondrial content by flow cytometry (left and central panels) and

of mtDNA copy number by qPCR (right panel) in WT and E336K cells. (**D)** Relative amount of steady-state mitochondrial complexes subunits measured by western blot. Cell protein extracts were separated by SDS-PAGE and probed with specific antibodies for actin, CI (anti-NDUFS3), CII (anti-SDHA), CIII (anti-1UQCRC1) and CIV (anti-MT-CO1). The amount of each protein was calculated relative to actin (right panel). Data are presented as mean ± SD of the mean. Sample sizes were as follows: n=5 technical replicates in **(A)**; n=6 (control) and n=8 (mutant) biological replicates in **(B)**; n=3 technical replicates (qPCR assay) and n=3 biological replicates (cytometry assay) in **(C)**; and n=4, 2, 2 and 3 biological replicates for CI, CIII, CIV and CII subunits, respectively, in **(D)**.

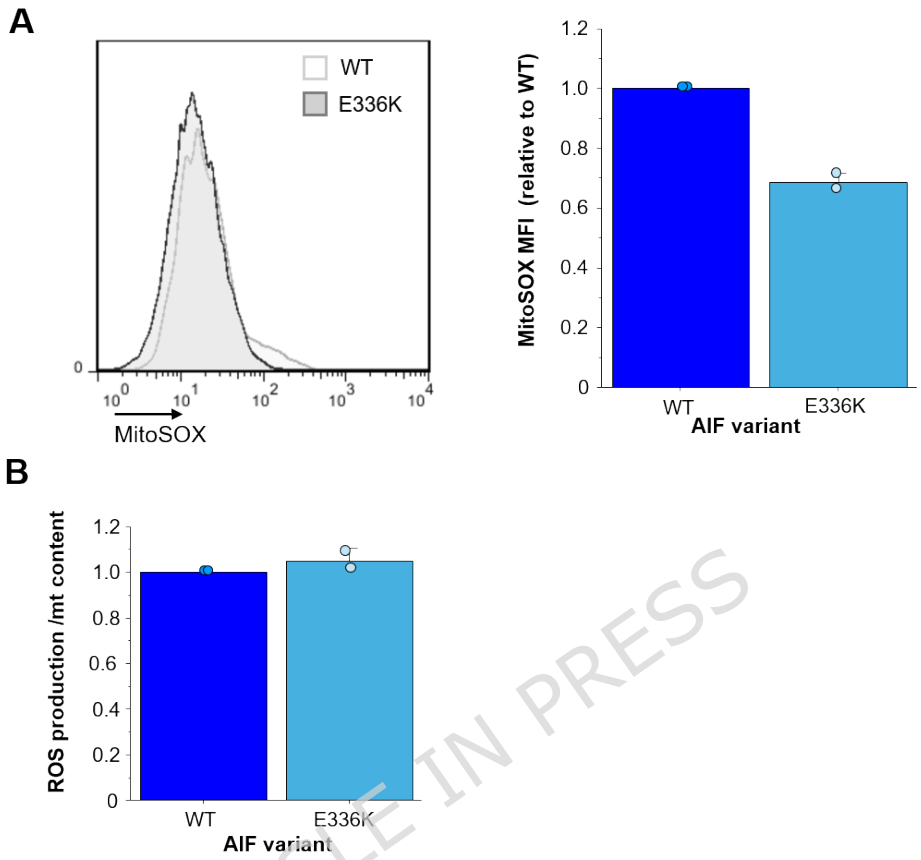

Fig. 4 Effect of the AIF E336K mutation on mitochondrial ROS production. (**A**) Evaluation of mitochondrial superoxide production by flow cytometry after MitoSOX™ staining. (**B**) Mitochondrial ROS production normalized by mitochondrial content in WT and E336K immortalized fibroblasts. Data are presented as mean ± SD of the mean; n=2 biological replicates.

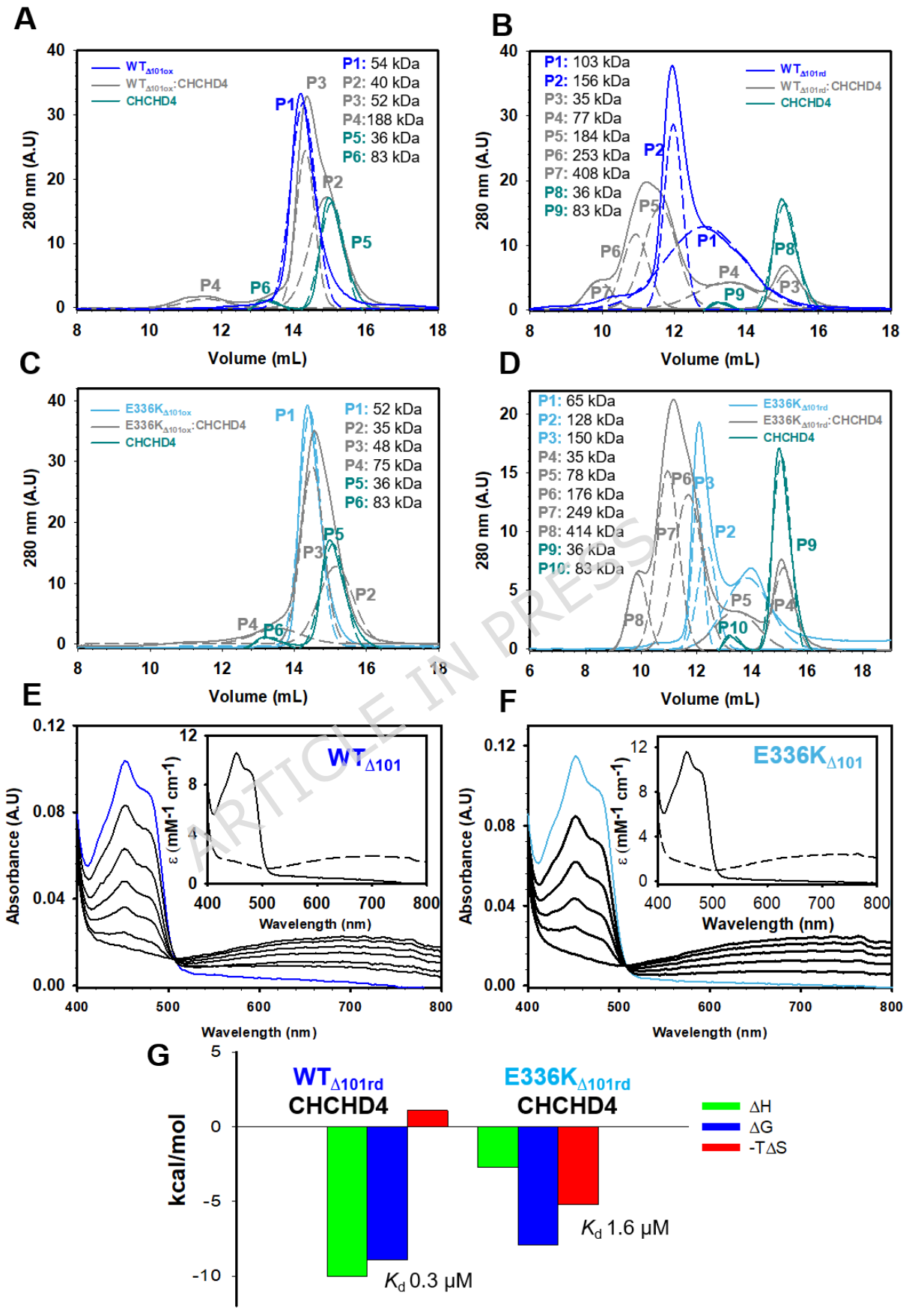

Fig. 5 Impact of E336K mutation on AIF molecular and redox properties. Influence on the stability of AIF complexes with CHCHD4. Elution profiles of $WT_{\Delta 101}$ (**A-B**) and $E336K_{\Delta 101}$ (**C-D**) variants in the absence and presence of a 3-fold molar excess of CHCHD4 and 2 mM NADH (A, C without NADH; and B, D with NADH). Control elution profiles of free $WT_{\Delta 101}$, $E336K_{\Delta 101}$, and CHCHD4 are shown as continuous blue, light blue and dark cyan lines, respectively. Elution profiles of $AIF_{\Delta 101}$:CHCHD4 mixtures are depicted as continuous dark grey lines. Gaussian analyses identify distinct populations corresponding to free $AIF_{\Delta 101}$ variants and CHCHD4 (colored dashed lines), and to $AIF_{\Delta 101}$:CHCHD4 complexes (dark grey dashed lines). (**E-F**) Spectral evolution of flavin reduction by NADH for $WT_{\Delta 101}$ and $E336K_{\Delta 101}$. Insets displayed simulated spectral species from global fitting to a single step (A→B) kinetic model. Initial spectra before NADH addition are shown in dark blue and light blue respectively for $WT_{\Delta 101}$ and $E336K_{\Delta 101}$. (**G**) Thermodynamic dissection of the interaction of NADH reduced $WT_{\Delta 101}$ and $E336K_{\Delta 101}$ AIF variants with CHCHD4, as assessed by ITC. Gibbs free energy (ΔG), enthalpy (ΔH) and entropy contributions ($-T\Delta S$) are shown in blue, green and red bars, respectively. For ITC $AIF_{\Delta 101}$:CHCHD4 binding assays, reduced forms of $AIF_{\Delta 101}$ variants were obtained by premixing the oxidized proteins and NADH at a 1:100 ratio. Assays were performed in triplicate.

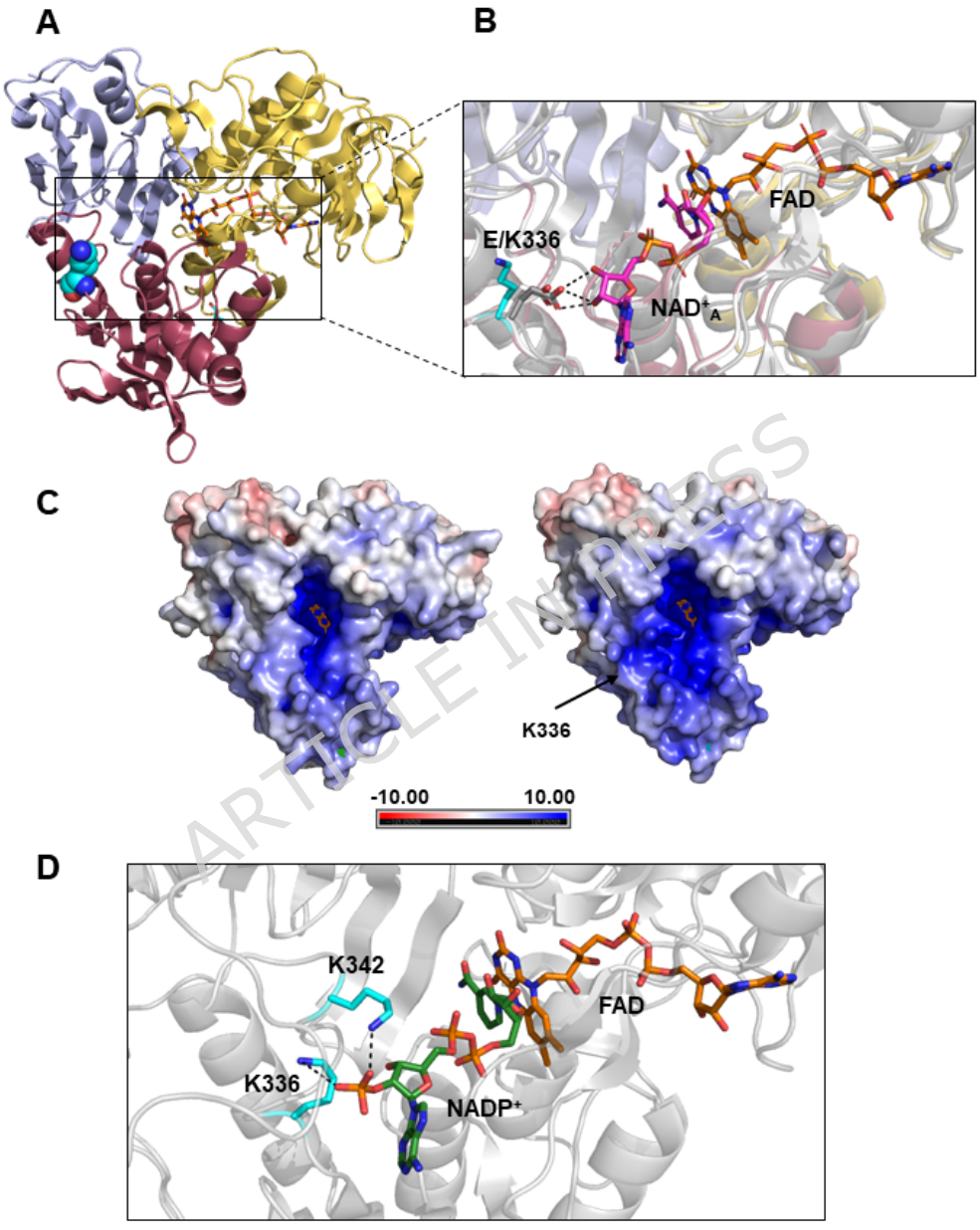

Fig. 6. Impact of the E336K mutation on the structural properties of AIF. (**A**) Overall structure of E336K $AIF_{\Delta 101ox}$ (PDB ID: 9SZQ), colored

according to domain type: NADH binding (yellow), FAD binding (raspberry red) and C-terminal (blue). The side chain of K336 is depicted as cyan C atom balls and the FAD cofactor as orange sticks. (**B**) Structural comparison of the point mutation site in $E336K_{\Delta101ox}$ (colors as in A, PDB ID: 9SZQ), $WT_{\Delta101ox}$ (white, PDB 4BV6) and $WT_{\Delta101rd}$:NAD^+ (grey, PDB ID: 4BUR, chain A). In the $WT_{\Delta101rd}$:NAD^+ complex, the NAD^+ coenzyme is shown as sticks with pink carbons. The side chain of residue 336 is shown as sticks, cyan when mutated, and white and grey respectively for $WT_{\Delta101}$ and $WT_{\Delta101rd}$:NAD^+. Dashed lines indicate the hydrogen bonds formed by E336 with the ribose of the adenine moiety of the coenzyme in the $WT_{\Delta101rd}$:NAD^+ complex. (**C**) Surface electrostatic potential of $WT_{\Delta101}$ (left) and the $E336K_{\Delta101}$ (right). Electrostatic surface potentials were calculated at pH 7.4 using APBS and PDB2PQR [11, 14, 27]. (**D**) Potential binding mode of the 2′P-adenine nucleotide moiety of $NADP^+$ in a putative $E336K_{\Delta101rd}$:$NADP^+$ structural model. K342 and K336 are displayed in sticks with carbon atoms in cyan.

To submit to Cell Communication and Signaling

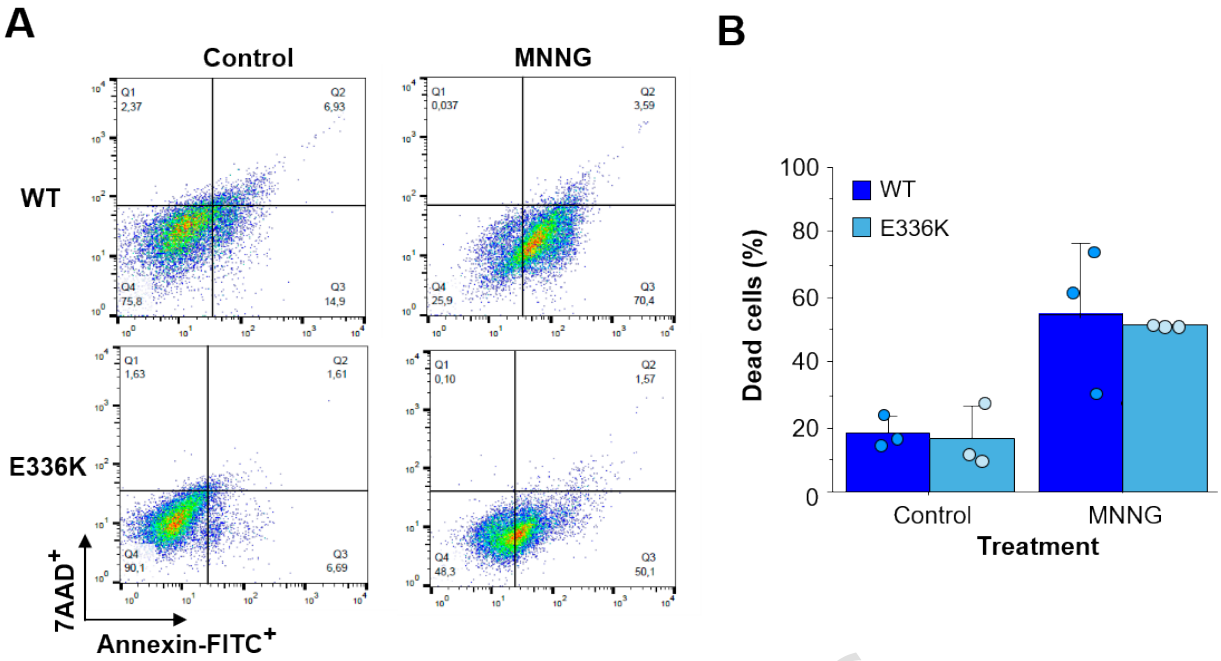

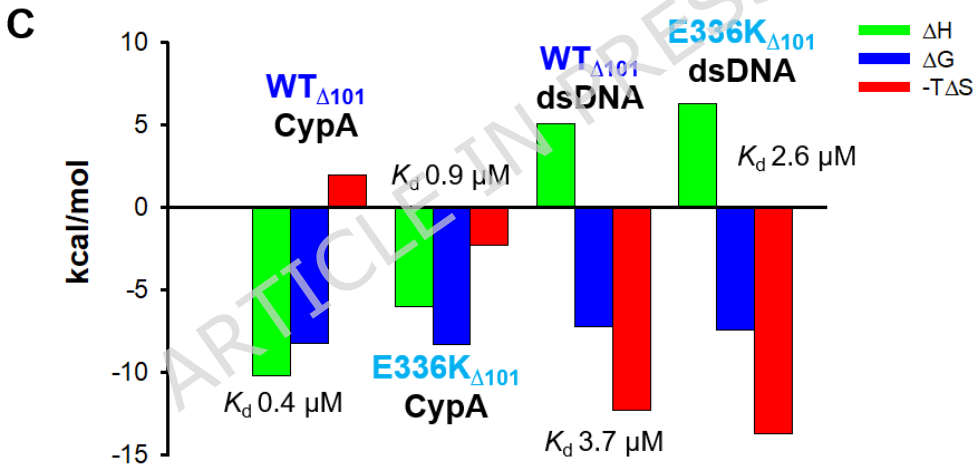

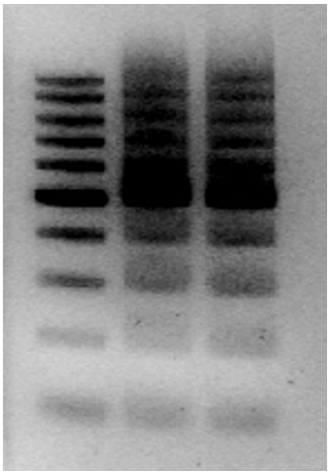

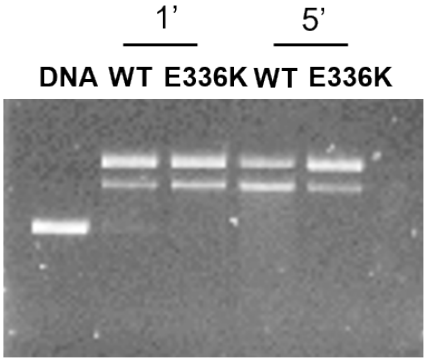

Fig 7. Impact of E336K mutation on AIF apoptotic function. (**A-B**) MNNG induced cell death in WT and E336K fibroblasts. Cell death was assessed by flow cytometry after simultaneous staining with Annexin V-FITC and 7-ADD in cells treated with MNNG. (**A**) Representative dot plots illustrating staining patterns in treated *vs* untreated WT and E336K cells. (**B**) Quantification of cell death after 20 minutes of MNNG exposure, 24 h prior to analysis. Data are presented as mean ± SD from three independent experiments (n=3 biological replicates). (**C**) Thermodynamic dissection of the interactions of $AIF_{\Delta 101ox}$ variants with CypA and dsDNA as assessed by ITC. Gibbs free energy (ΔG), enthalpy (ΔH) and entropy contributions ($-T\Delta S$) are shown in blue, green and red bars, respectively. (**D**) Effect of E336K mutation in DNA retention by AIF. Electrophoretic mobility shift assays (EMSAs) were performed using 6 µg of $WT_{\Delta 101}$ or its $E336K_{\Delta 101}$ variant with 500 ng of 100 bp dsDNA ladder (Thermo Scientific). Incubations were carried out for 30 min at 25 ºC in 50 mM potassium phosphate buffer, pH 7.4. Mixtures were resolved on a 1 % agarose gel electrophoresis and visualized using SYBR™ Safe. As a control, the dsDNA ladder (D) was incubated without the protein under the same conditions. (**E**) Time course of the E336K mutation effect on AIF nuclease activity. A total of 250 ng of double-stranded supercoiled pcDNA3.1 plasmid was incubated with 250 ng of $WT_{\Delta 101}$ or $E336K_{\Delta 101}$ in 20 mM Tris/HCl buffer, pH 8.0, supplemented with 0.1 mM $CaCl_2$ and 1 mM $MgCl_2$ at 30 ºC for either 1 or 5 minutes. As a control, the plasmid was incubated without the

protein under the same conditions. Samples were separated by electrophoresis on a 0.7 % agarose gel and visualized by SYBR™ Safe.

References

1 Acin-Perez R, Bayona-Bafaluy MP, Bueno M, Machicado C, Fernandez-Silva P, Perez-Martos A, Montoya J, Lopez-Perez MJ, Sancho J, Enriquez JA (2003) An intragenic suppressor in the cytochrome c oxidase I gene of mouse mitochondrial DNA. Hum Mol Genet 12: 329-339 Doi 10.1093/hmg/ddg021

2 Acin-Perez R, Fernandez-Silva P, Peleato ML, Perez-Martos A, Enriquez JA (2008) Respiratory active mitochondrial supercomplexes. Mol Cell 32: 529-539 Doi 10.1016/j.molcel.2008.10.021

3 Afonine PV, Grosse-Kunstleve RW, Echols N, Headd JJ, Moriarty NW, Mustyakimov M, Terwilliger TC, Urzhumtsev A, Zwart PH, Adams PD (2012) Towards automated crystallographic structure refinement with phenix.refine. Acta Crystallogr D Biol Crystallogr 68: 352-367 Doi 10.1107/S0907444912001308

4 Ardissone A, Piscosquito G, Legati A, Langella T, Lamantea E, Garavaglia B, Salsano E, Farina L, Moroni I, Pareyson Det al (2015) A slowly progressive mitochondrial encephalomyopathy widens the spectrum of AIFM1 disorders. Neurology 84: 2193-2195 Doi 10.1212/WNL.0000000000001613

5 Artus C, Boujrad H, Bouharrour A, Brunelle MN, Hoos S, Yuste VJ, Lenormand P, Rousselle JC, Namane A, England Pet al (2010) AIF promotes chromatinolysis and caspase-independent programmed necrosis by interacting with histone H2AX. EMBO J 29: 1585-1599 Doi 10.1038/emboj.2010.43

6 Bano D, Prehn JHM (2018) Apoptosis-Inducing Factor (AIF) in Physiology and Disease: The Tale of a Repented Natural Born Killer. EBioMedicine 30: 29-37 Doi 10.1016/j.ebiom.2018.03.016

7 Bogdanova-Mihaylova P, Alexander MD, Murphy RP, Chen H, Healy DG, Walsh RA, Murphy SM (2019) Clinical spectrum of AIFM1-associated disease in an Irish family, from mild neuropathy to severe cerebellar ataxia with colour blindness. J Peripher Nerv Syst 24: 348-353 Doi 10.1111/jns.12348

8 Brosey CA, Ho C, Long WZ, Singh S, Burnett K, Hura GL, Nix JC, Bowman GR, Ellenberger T, Tainer JA (2016) Defining NADH-Driven Allostery Regulating Apoptosis-Inducing Factor. Structure: Doi 10.1016/j.str.2016.09.012

9 Brosey CA, Shen R, Tainer JA (2025) NADH-bound AIF activates the mitochondrial CHCHD4/MIA40 chaperone by a substrate-mimicry mechanism. EMBO J. © 2025. The Author(s). City

10 Cowchock FS, Duckett SW, Streletz LJ, Graziani LJ, Jackson LG (1985) X-linked motor-sensory neuropathy type-II with deafness and mental retardation: a new disorder. Am J Med Genet 20: 307-315 Doi 10.1002/ajmg.1320200214

11 Delano WL (2002) PyMOL: an open-source molecular graphics tool. CCP4 Newsletter On Protein Crystallography 40: 82-92

12 Delavallee L, Mathiah N, Cabon L, Mazeraud A, Brunelle-Navas MN, Lerner LK, Tannoury M, Prola A, Moreno-Loshuertos R, Baritaud Met al (2020) Mitochondrial AIF loss causes metabolic reprogramming, caspase-independent cell death blockade, embryonic lethality, and perinatal hydrocephalus. Mol Metab 40: 101027 Doi 10.1016/j.molmet.2020.101027

13 Delavallée L, Mathiah N, Cabon L, Mazeraud A, Brunelle-Navas MN, Lerner LK, Tannoury M, Prola A, Moreno-Loshuertos R, Baritaud Met al (2020) Mitochondrial AIF loss causes metabolic reprogramming, caspase-independent cell death blockade, embryonic lethality, and perinatal hydrocephalus. Mol Metab: 101027 Doi 10.1016/j.molmet.2020.101027

14 Dolinsky TJ, Nielsen JE, McCammon JA, Baker NA (2004) PDB2PQR: an automated pipeline for the setup of Poisson-Boltzmann electrostatics calculations. Nucleic Acids Res 32: W665-667 Doi 10.1093/nar/gkh381

15 Emsley P, Lohkamp B, Scott WG, Cowtan K (2010) Features and development of Coot. Acta Crystallogr D Biol Crystallogr 66: 486-501 Doi 10.1107/S0907444910007493

16 Evans P (2006) Scaling and assessment of data quality. Acta Crystallogr D Biol Crystallogr 62: 72-82 Doi 10.1107/S0907444905036693

17 Fagnani E, Cocomazzi P, Pellegrino S, Tedeschi G, Scalvini FG, Cossu F, Da Vela S, Aliverti A, Mastrangelo E, Milani M (2024) CHCHD4 binding affects the active site of apoptosis inducing factor (AIF): Structural determinants for allosteric regulation. Structure. © 2024 The Author(s). Published by Elsevier Inc, City, pp 594-602 e594

18 Farina B, Di Sorbo G, Chambery A, Caporale A, Leoni G, Russo R, Mascanzoni F, Raimondo D, Fattorusso R, Ruvo Met al (2017) Structural and biochemical insights of CypA and AIF interaction. Sci Rep 7: 1138 Doi 10.1038/s41598-017-01337-8

19 Farina B, Sturlese M, Mascanzoni F, Caporale A, Monti A, Di Sorbo G, Fattorusso R, Ruvo M, Doti N (2018) Binding mode of AIF(370-394) peptide to CypA: insights from NMR, label-free and molecular docking studies. Biochem J 475: 2377-2393 Doi 10.1042/BCJ20180177

20 Ferreira P, Villanueva R, Martinez-Julvez M, Herguedas B, Marcuello C, Fernandez-Silva P, Cabon L, Hermoso JA, Lostao A, Susin SAet al (2014) Structural insights into the coenzyme mediated monomer-dimer transition of the pro-apoptotic apoptosis inducing factor. Biochemistry 53: 4204-4215 Doi 10.1021/bi500343r

21 Ghezzi D, Sevrioukova I, Invernizzi F, Lamperti C, Mora M, D'Adamo P, Novara F, Zuffardi O, Uziel G, Zeviani M (2010) Severe X-linked mitochondrial encephalomyopathy associated with a mutation in apoptosis-inducing factor. Am J Hum Genet 86: 639-649 Doi 10.1016/j.ajhg.2010.03.002

22 Hangen E, Feraud O, Lachkar S, Mou H, Doti N, Fimia GM, Lam NV, Zhu C, Godin I, Muller Ket al (2015) Interaction between AIF and CHCHD4 Regulates Respiratory Chain Biogenesis. Mol Cell 58: 1001-1014 Doi 10.1016/j.molcel.2015.04.020

23 Heimer G, Eyal E, Zhu X, Ruzzo EK, Marek-Yagel D, Sagiv D, Anikster Y, Reznik-Wolf H, Pras E, Oz Levi Det al (2018) Mutations in AIFM1 cause an X-linked childhood cerebellar ataxia partially responsive to riboflavin. Eur J Paediatr Neurol 22: 93-101 Doi 10.1016/j.ejpn.2017.09.004

24 Hofhaus G, Shakeley RM, Attardi G (1996) Use of polarography to detect respiration defects in cell cultures. Methods Enzymol 264: 476-483 Doi 10.1016/s0076-6879(96)64043-9

25 Hu B, Wang M, Castoro R, Simmons M, Dortch R, Yawn R, Li J (2017) A novel missense mutation in AIFM1 results in axonal polyneuropathy and misassembly of OXPHOS complexes. Eur J Neurol 24: 1499-1506 Doi 10.1111/ene.13452

26 Joza N, Susin SA, Daugas E, Stanford WL, Cho SK, Li CY, Sasaki T, Elia AJ, Cheng HY, Ravagnan Let al (2001) Essential role of the mitochondrial apoptosis-inducing factor in programmed cell death. Nature 410: 549-554 Doi 10.1038/35069004

27 Jurrus E, Engel D, Star K, Monson K, Brandi J, Felberg LE, Brookes DH, Wilson L, Chen J, Liles Ket al (2018) Improvements to the APBS biomolecular solvation software suite. Protein Sci 27: 112-128 Doi 10.1002/pro.3280

28 Kabsch W (2010) Xds. Acta Crystallogr D Biol Crystallogr 66: 125-132 Doi 10.1107/S0907444909047337

29 Klein JA, Longo-Guess CM, Rossmann MP, Seburn KL, Hurd RE, Frankel WN, Bronson RT, Ackerman SL (2002) The harlequin mouse mutation downregulates apoptosis-inducing factor. Nature 419: 367-374 Doi 10.1038/nature01034

30 McCoy AJ, Grosse-Kunstleve RW, Adams PD, Winn MD, Storoni LC, Read RJ (2007) Phaser crystallographic software. J Appl Crystallogr 40: 658-674 Doi 10.1107/S0021889807021206

31 Meyer K, Buettner S, Ghezzi D, Zeviani M, Bano D, Nicotera P (2015) Loss of apoptosis-inducing factor critically affects MIA40 function. Cell Death Dis 6: e1814 Doi 10.1038/cddis.2015.170

32 Miyake N, Wolf NI, Cayami FK, Crawford J, Bley A, Bulas D, Conant A, Bent SJ, Gripp KW, Hahn Aet al (2017) X-linked hypomyelination with spondylometaphyseal dysplasia (H-SMD) associated with mutations in AIFM1. Neurogenetics 18: 185-194 Doi 10.1007/s10048-017-0520-x

33 Mosmann T (1983) Rapid colorimetric assay for cellular growth and survival: application to proliferation and cytotoxicity assays. J Immunol Methods, City, pp 55-63

34 Murshudov GN, Vagin AA, Dodson EJ (1997) Refinement of macromolecular structures by the maximum-likelihood method. Acta Crystallogr D Biol Crystallogr 53: 240-255 Doi 10.1107/S0907444996012255

35 Mussulini BHM, Maruszczak KK, Draczkowski P, Borrero-Landazabal MA, Ayyamperumal S, Wnorowski A, Wasilewski M, Chacinska A (2025) MIA40 suppresses cell death induced by apoptosis-inducing factor 1. EMBO Rep. © 2025. The Author(s). City

36 Novo N, Romero-Tamayo S, Marcuello C, Boneta S, Blasco-Machin I, Velazquez-Campoy A, Villanueva R, Moreno-Loshuertos R, Lostao A, Medina Met al (2023) Beyond a platform protein for the degradosome assembly: The Apoptosis-Inducing Factor as an efficient nuclease involved in chromatinolysis. PNAS Nexus 2: pgac312 Doi 10.1093/pnasnexus/pgac312

37 Pandolfo M, Rai M, Remiche G, Desmyter L, Vandernoot I (2020) Cerebellar ataxia, neuropathy, hearing loss, and intellectual disability due to AIFM1 mutation. Neurol Genet 6: e420 Doi 10.1212/NXG.0000000000000420

38 Reinhardt C, Arena G, Nedara K, Edwards R, Brenner C, Tokatlidis K, Modjtahedi N (2020) AIF meets the CHCHD4/Mia40-dependent

mitochondrial import pathway. Biochim Biophys Acta Mol Basis Dis 1866: 165746 Doi 10.1016/j.bbadis.2020.165746

39 Richards S, Aziz N, Bale S, Bick D, Das S, Gastier-Foster J, Grody WW, Hegde M, Lyon E, Spector Eet al (2015) Standards and guidelines for the interpretation of sequence variants: a joint consensus recommendation of the American College of Medical Genetics and Genomics and the Association for Molecular Pathology. Genet Med 17: 405-424 Doi 10.1038/gim.2015.30

40 Rinaldi C, Grunseich C, Sevrioukova IF, Schindler A, Horkayne-Szakaly I, Lamperti C, Landoure G, Kennerson ML, Burnett BG, Bonnemann Cet al (2012) Cowchock syndrome is associated with a mutation in apoptosis-inducing factor. Am J Hum Genet 91: 1095-1102 Doi 10.1016/j.ajhg.2012.10.008

41 Romero-Tamayo S, Laplaza R, Velazquez-Campoy A, Villanueva R, Medina M, Ferreira P (2021) W196 and the *β*-Hairpin Motif Modulate the Redox Switch of Conformation and the Biomolecular Interaction Network of the Apoptosis-Inducing Factor. Oxid Med Cell Longev 2021: 6673661 Doi 10.1155/2021/6673661

42 Salscheider SL, Gerlich S, Cabrera-Orefice A, Peker E, Rothemann RA, Murschall LM, Finger Y, Szczepanowska K, Ahmadi ZA, Guerrero-Castillo Set al (2022) AIFM1 is a component of the mitochondrial disulfide relay that drives complex I assembly through efficient import of NDUFS5. EMBO J 41: e110784

43 Sancho J (2013) The stability of 2-state, 3-state and more-state proteins from simple spectroscopic techniques... plus the structure of the equilibrium intermediates at the same time. Arch Biochem Biophys 531: 4-13 Doi 10.1016/j.abb.2012.10.014

44 Sancho P, Sanchez-Monteagudo A, Collado A, Marco-Marin C, Dominguez-Gonzalez C, Camacho A, Knecht E, Espinos C, Lupo V (2017) A newly distal hereditary motor neuropathy caused by a rare AIFM1 mutation. Neurogenetics 18: 245-250 Doi 10.1007/s10048-017-0524-6

45 Schagger H (1995) Native electrophoresis for isolation of mitochondrial oxidative phosphorylation protein complexes. Methods Enzymol 260: 190-202 Doi 10.1016/0076-6879(95)60137-6

46 Sevrioukova IF (2016) Structure/Function Relations in AIFM1 Variants Associated with Neurodegenerative Disorders. J Mol Biol 428: 3650-3665 Doi 10.1016/j.jmb.2016.05.004

47 Susin SA, Lorenzo HK, Zamzami N, Marzo I, Snow BE, Brothers GM, Mangion J, Jacotot E, Costantini P, Loeffler Met al (1999) Molecular characterization of mitochondrial apoptosis-inducing factor. Nature 397: 441-446 Doi 10.1038/17135

48 Tiranti V, Munaro M, Sandona D, Lamantea E, Rimoldi M, DiDonato S, Bisson R, Zeviani M (1995) Nuclear DNA origin of cytochrome c oxidase deficiency in Leigh's syndrome: genetic evidence based on patient's-derived rho° transformants. Hum Mol Genet 4: 2017-2023 Doi 10.1093/hmg/4.11.2017

49 Tunyi J, Abreu NJ, Tripathi R, Mathew MT, Mears A, Agrawal P, Thakur V, Rezai AR, Reyes EL (2023) Deep Brain Stimulation for the Management of AIFM1-Related Disabling Tremor: A Case Series. Pediatr Neurol. © 2023 Elsevier Inc, City, pp 47-50

50 Vahsen N, Cande C, Briere JJ, Benit P, Joza N, Larochette N, Mastroberardino PG, Pequignot MO, Casares N, Lazar Vet al (2004) AIF

deficiency compromises oxidative phosphorylation. EMBO J 23: 4679-4689 Doi 10.1038/sj.emboj.7600461

51 Vasquez A, Schimmenti LA, Demirel N, Rabatin AE, Fischer CR, Pinto MV, Boesch RP, Selcen D (2024) Novel AIFM1 Variant in 2 Siblings With Sensorineural Hearing Loss and Cerebellar Ataxia. Neurol Genet 10: e200216 Doi 10.1212/NXG.0000000000200216

52 Villanueva R, Romero-Tamayo S, Laplaza R, Martinez-Olivan J, Velazquez-Campoy A, Sancho J, Ferreira P, Medina M (2019) Redox- and Ligand Binding-Dependent Conformational Ensembles in the Human Apoptosis-Inducing Factor Regulate Its Pro-Life and Cell Death Functions. Antioxid Redox Signal 30: 2013-2029 Doi 10.1089/ars.2018.7658

53 Wang B, Li X, Wang J, Liu L, Xie Y, Huang S, Pakhrin PS, Jin Q, Zhu C, Tang Bet al (2018) A novel AIFM1 mutation in a Chinese family with X-linked Charcot-Marie-Tooth disease type 4. Neuromuscul Disord. © 2018 Elsevier B.V, City, pp 652-659

54 Wang C, Lin Z, Yuan Z, Tang T, Fan L, Liu Y, Wu X (2023) Whole-exome sequencing detected a novel AIFM1 variant in a Han-Chinese family with Cowchock syndrome. Hereditas 160: 22 Doi 10.1186/s41065-023-00282-z

55 Winn MD, Ballard CC, Cowtan KD, Dodson EJ, Emsley P, Evans PR, Keegan RM, Krissinel EB, Leslie AG, McCoy Aet al (2011) Overview of the CCP4 suite and current developments. Acta Crystallogr D Biol Crystallogr 67: 235-242 Doi 10.1107/S0907444910045749

56 Wischhof L, Scifo E, Ehninger D, Bano D (2022) AIFM1 beyond cell death: An overview of this OXPHOS-inducing factor in mitochondrial diseases. EBioMedicine 83: 104231 Doi 10.1016/j.ebiom.2022.104231

57 Zhao Y, Lin Y, Wang B, Liu F, Zhao D, Wang W, Ren H, Wang J, Xu Z, Yan Cet al (2023) A Missense Variant in AIFM1 Caused Mitochondrial Dysfunction and Intolerance to Riboflavin Deficiency. Neuromolecular Med. © 2023. The Author(s), under exclusive licence to Springer Science+Business Media, LLC, part of Springer Nature., City, pp 489-500

58 Zong L, Guan J, Ealy M, Zhang Q, Wang D, Wang H, Zhao Y, Shen Z, Campbell CA, Wang Fet al (2015) Mutations in apoptosis-inducing factor cause X-linked recessive auditory neuropathy spectrum disorder. J Med Genet 52: 523-531 Doi 10.1136/jmedgenet-2014-102961

Table 1. Summary of previously reported pathogenic *AIFM1* variants associated to Charcot-Marie-Tooth disease type 4 (CMTX4/COWCHOCK)

Mutation	Disease onset	Progression	Phenotypes	Domain	Protein level	OXPHOS activity	Redox activity	Cell death	Ref.
COWCHOCK syndrome									
T141I	4.5y	Slow	Childhood-onset cerebellar ataxia with auditory neuropathy, axonal sensorimotor neuropathy and cardiomyopathy	FAD-binding	---	---	---	---	[23]
M171I	5-11y	Slow	Childhood-onset slowly progressive axonal motor and sensory neuropathy, lower limb weakness and atrophy, steppage gait, pes cavus, absence of CNS symptoms or cognitive impairment.	FAD-binding	---	Abnormal mitochondrial morphology and accumulation in nerve and muscle suggest mitochondrial dysfunction	----	----	[53]
F210L	14y	Slow	Distal muscle atrophy and weakness (particularly ankle flexors), absent ankle reflexes, and mild sensory impairment. No involvement of central nervous system or other organs.	FAD-binding	Normal	Misassemble of Complex I and Complex III (~80% reduction)	----	No effect; normal interaction with HSP70 (inhibitor of AIF nuclear translocation)	[25]
F210S	16-18m	Slow, but severe progression	Early-onset axonal polyneuropathy with exclusive motor fiber involvement. Sensory nerves were unaffected. Cognitive function and cranial nerves were normal. Severe distal weakness and muscle atrophy with mild to moderate proximal weakness.	FAD-binding	Reduced (normal mRNA expression)	Mitochondrial fragmentation and reduced interconnectivity suggest mitochondrial dysfunction	---	Not altered	[44]
G262S	1y	Slow	Mitochondrial encephalomyopathy characterized by ataxia (sensory and cerebellar), hearing loss, cognitive impairment, visual loss, distal muscle weakness, and neuropathy.	FAD-binding	Strong reduction; less stability	Reduced Complex IV activity, partial reduction of other complexes	Reduced NADH affinity, increased NADH oxidation, destabilized CTC	----	[4, 46]
L311V	10y	Slow	Severe axonal sensorimotor neuropathy, distal muscle atrophy and weakness, pes cavus, sensorineural hearing loss, cognitive decline, and scoliosis	NADH-binding	Predicted destabilization	----	----	---	[54]

G399S	2y	Slow	Cerebellar ataxia and atrophy and dysarthria, sensorineural hearing loss, intellectual disability, axonal peripheral neuropathy, and mood and behavioral disorders.	NADH-binding	Normal	---	---	---	[37]

Table 1. Continued

M340T	5 y	Slow	Childhood-onset cerebellar ataxia with auditory neuropathy, axonal sensorimotor neuropathy	NADH-binding	Reduced	Reduced Complex I, II and IV. $\Delta\Psi_m$ decreased.	---	Reduced, impaired	[7, 23, 57]
I433M	5y,13y	Rapid, Slow	Neurodegenerative syndrome with hearing loss, ataxia, neuropathy, and optic atrophy.	FAD-binding	---	---	---	---	[51]
E493V	Early age	Slow	Axonal motor and sensory neuropathy, bilateral sensorineural hearing loss, cognitive impairment, distal muscle wasting and weakness (lower > upper limbs)	C-terminal	Normal level but reduced stability	No affected	Increased NADH oxidation, destabilized CTC	Enhanced	[40, 46, 52]
H457Y	3y, 4y	Slow	Complex progressive movement disorder. Features included cerebellar ataxia, disabling cerebellar tremor, sensorineural hearing loss, sensory polyneuropathy, language, fine motor delays, dystonia and optic nerve hypoplasia	C-terminal	---	---	---	---	[49]

NA: not available; d: days; m: months; y, year; ---: not studied; $\Delta\Psi_m$: mitochondrial membrane potential

Table 2. Neurophysiological findings in patient holding the E336K AIF mutation

Nerve/muscle	Study type	Findings	Clinical Interpretation
Nerve Sural R/L	Sensory	No response	Severe sensory impairment
Nerve Superficial peroneal R/L	Sensory	No response	Severe sensory impairment
Nerve Median sensory R	Sensory	Lat 3.45 ms | Amp 1.8 µV | Vel 46.4 m/s	Moderate sensory neuropathy
Nerve Ulnar sensory R	Sensory	Lat 2.55 ms | Amp 4.7 µV | Vel 47.1 m/s	Moderate sensory neuropathy
Nerve Median motor R	Motor	Lat 4.30–8.40 ms | Amp 7.8–8.2 mV | Vel 59.8 m/s	Mild to moderate motor neuropathy
Nerve Ulnar motor R	Motor	Lat 3.35–9.55 ms | Amp 11.0–7.6 mV | Vel 65.4 / 44.4 m/s	Mild motor neuropathy
Nerve Common peroneal R/L	Motor	No response	Severe motor neuropathy
Nerve Tibial R/L	Motor	No response	Severe motor neuropathy
Muscle Tibialis anterior R	EMG	Normal IA, no spontaneous activity, Mixed I recruitment	Axonal damage, no denervation, altered recruitment
Muscle Gastrocnemius med. R	EMG	Normal IA, no spontaneous activity, Mixed I recruitment	Axonal damage, no denervation, altered recruitment
Muscle Tibialis anterior L	EMG	Normal IA, no spontaneous activity, Mixed I recruitment	Axonal damage, no denervation, altered recruitment
Muscle Gastrocnemius med. L	EMG	Normal IA, no spontaneous activity, Mixed I recruitment	Axonal damage, no denervation, altered recruitment
Muscle Vastus medialis R	EMG	Normal IA, no spontaneous activity, Mixed II recruitment	Axonal damage, no denervation, altered recruitment
MuscleVastus medialis L	EMG	Normal IA, no spontaneous activity, Mixed II recruitment	Axonal damage, no denervation, altered recruitment
Muscle Biceps R	EMG	Normal IA, no spontaneous activity, Mixed III recruitment	Axonal damage, no denervation, altered recruitment
Muscle Abductor digiti minimi (ulnar) R	EMG	Normal IA, no spontaneous activity, Mixed III recruitment	Axonal damage, no denervation, altered recruitment

Summary of motor and sensory nerve conduction studies and electromyographic evaluation. The results demonstrate a severe, length-dependent, axonal sensorimotor polyneuropathy, consistent with Charcot-Marie-Tooth disease type X4 (CMTX4, Cowchock syndrome). EMG: electromyography; IA: insertion activity.

Table 3. Audiometric findings before and after cochlear implantation in patient holding the E336K AIF mutation

Parameter	Pre-implant	Post-implant (Right Cochlear Implant)
Hearing thresholds	Severe-to-profound bilateral sensorineural hearing loss (≈90% by age 41)	Clear improvement in free-field thresholds
Hearing aids	Required since age 25, with limited benefit	Not required, replaced by CI
Sentence comprehension	Severely impaired	≈90% sentence comprehension with implant
Speech recognition	Minimal, lip-reading required	Significantly improved with combination of lip-reading + implant
Left ear outcome	Profound hearing loss, no functional benefit	Persistent profound hearing loss, no functional benefit
Overall functional outcome	Severe bilateral anacrusis	Partial functional recovery with right CI

Summary of the most relevant parameters, including hearing thresholds, speech comprehension, and functional outcomes. Marked improvement was observed after right cochlear implantation, with partial recovery of auditory performance despite persistent profound hearing loss in the left ear. CI: cochlear implant.

Table 4. Steady-state kinetic parameters of $AIF_{\Delta 101}$ variants with NADH and NADPH as hydride donors

Variants	**NADH**			**NADPH**			**Specificity**
	k_{cat} **(s^{-1})**	K_m^{NADH} **(mM)**	k_{cat}/K_m^{NADH} **(s^{-1} mM^{-1})**	k_{cat} **(s^{-1})**	K_m^{NADPH} **(mM)**	k_{cat}/K_m^{NADPH} **(s^{-1} mM^{-1})**	**NADH/NADPH efficiency**
$WT_{\Delta 101}$	2.0 ± 0.1	0.5 ± 0.1	4.0 ± 1	0.02 ± 0.01	0.5 ± 0.1	0.04 ± 0.02	75
$E336K_{\Delta 101}$	2.5 ± 0.1	2.8 ± 0.5	0.9 ± 0.2	4.9 ± 0.1	0.12 ± 0.01	40 ± 4	0.0225

Assays were performed using DCPIP as hydride acceptor at 25 ºC in 50 mM potassium phosphate, pH 7.4. (n=3, mean ± SD);

Table 5. Pre-steady state kinetic parameters of $AIF_{\Delta 101}$ variants with NADH as hydride donor

Variants	**Pre-steady-sate**			**CTC**
	k_{HT} **(s^{-1})**	K_d^{NADH} **(mM)**	k_{HT}/K_d^{NADH} **(s^{-1} mM^{-1})**	**Half-life (min)**
$WT_{\Delta 101}$	1.1 □ 0.1	4.3 □ 0.1	0.30 +0.03	20
$E336K_{\Delta 101}$	2.9 ± 0.1	13.4 ± 0.1	0.20 ± 0.01	NS

Assays were performed at 25 ºC in 50 mM potassium phosphate, pH 7.4. (n=3, mean ± SD); NS: not stabilized under assayed conditions.